MJO impacts on South America and their modulation by ENSO in MetUM-GOML3 model

L. G. Fernandes[1,4,†], A. M. Grimm[1,2], and N. P. Klingaman[3,4]

[1]Postgraduate Program in Water Resources and Environmental Engineering, Federal University of Parana (UFPR), Curitiba, Paraná, Brazil

[2]Department of Physics, Federal University of Parana (UFPR), Curitiba, Paraná, Brazil

[3]National Centre for Atmospheric Science, University of Reading, Reading, United Kingdom

[4]Department of Meteorology, University of Reading, Reading, United Kingdom

Corresponding author: Laís G. Fernandes (lais.fernandes@pdx.edu)

†Fernandes' current affiliation: Department of Geography, Portland State University, Portland, Oregon, United States

Key Points:

- The model simulates well the MJO opposite patterns in the teleconnections to SA in phases 8 and 4 and their impacts.
- The model reproduces the ENSO effects on the basic state and MJO convection, which modulate the MJO teleconnections to SA.
- Simulations show the nonlinear ENSO effect on the MJO teleconnections and its impacts on South American rainfall.

Abstract

The impacts of the Madden-Julian Oscillation (MJO) on the South American monsoon season (December-February) and possible changes during El Niño (EN) and La Niña (LN) events are analyzed in the UK Met Office Unified Model Global Ocean Mixed Layer configuration (MetUM-GOML3). Experiments sixty years long, with and without El Niño-Southern Oscillation (ENSO), considering different spatial resolutions, are performed to assess if ENSO influences several MJO characteristics, including the teleconnections to South America (SA). Simulations without ENSO show: (i) an extratropical teleconnection triggered by enhanced convection in the central-east subtropical South Pacific (CSSP) and its strongest impact on central-east South American precipitation in phase 8, earlier than in observations (phase 1). (ii) An extratropical teleconnection, triggered by suppressed convection over the same region, with strongest impact on South American precipitation in phase 4, with opposite sign. (iii) Increased resolution enhances the MJO convection and the South American circulation-precipitation dipole. ENSO affects the basic state and the MJO convection, which modulate teleconnections to SA in simulations with ENSO cycles. EN (LN) strengthens (deteriorates) MJO propagation and its convection. However, both EN and LN produce enhanced convection over the CSSP in phase 8. The extratropical teleconnections and their impacts are stronger under ENSO with respect to those in simulations without ENSO. Hence, both simulated ENSO states generate forcing that more efficiently triggers teleconnections than simulations without ENSO, indicating nonlinear ENSO effects on MJO anomalies over SA.

Plain Language Summary

This investigation assesses changes produced by the active phases of the El Niño-Southern Oscillation (ENSO) phenomenon (El Niño and La Niña) on the Madden-Julian Oscillation (MJO) and its impacts on precipitation over South America (SA) in the Met Office Global Ocean Mixed Layer Model, known for simulating ENSO and MJO well. Simulations show that El Niño and La Niña basic states influence the MJO phase distribution, eastward propagation, the position and intensity of the MJO convection, teleconnections, and impacts on South American rainfall. El Niño strengthens the MJO convection and propagation, while La Niña deteriorates these MJO characteristics, as pointed out by previous studies. However, both active ENSO states support better simulation of MJO convection over the central-east subtropical South Pacific (CSSP), that trigger MJO teleconnections impacting South American rainfall. When the model improves the simulation of the MJO teleconnections, the precipitation patterns over SA are also better simulated. As the El Niño background flow improves both MJO and its teleconnections to SA, other global climate models that simulate ENSO and MJO may also reproduce these MJO features, improving subseasonal to seasonal (S2S) predictions to SA in the austral summer monsoon season.

1 Introduction

The Madden-Julian Oscillation (MJO), the leading global intraseasonal climate variability mode (Zhang, 2005), has a substantial role in austral summer (December-January-February, DJF) rainfall variability in South America (SA) (Alvarez et al., 2015; Grimm, 2019). The MJO influences South American rainfall through tropical (Kelvin and Rossby equatorial waves) and extratropical (extratropical Rossby waves) teleconnections (Grimm, 2019). The former affects anomalous precipitation in equatorial SA and tropical central-east SA (CESA); the latter affects the rainfall anomalies over subtropical CESA, where the South Atlantic Convergence Zone (SACZ) develops on the eastern edge of the monsoon core region, and subtropical southeastern SA (SESA) (Grimm, 2019).

Although the El Niño-Southern Oscillation (ENSO) does not affect overall MJO activity (Hendon et al., 1999; Slingo et al., 1999), El Niño events expand the MJO domain eastward in the central Pacific (Hendon et al., 1999; Kessler, 2001; Tam & Lau, 2005; Wei & Ren, 2019). This is a critical region for SA as the MJO convection starts to weaken and shifts south, entering the central-east subtropical South Pacific (CSSP), where it is most efficient to trigger the extratropical teleconnection to SA (Grimm, 2019; Grimm & Silva Dias, 1995).

Fernandes and Grimm (2023) described the ENSO-driven modulation of the MJO impacts on SA. They noted that El Niño (EN) and La Niña (LN) effects on MJO impacts, with respect to neutral ENSO, are not always opposite, indicating nonlinear effects of ENSO on MJO anomalies over SA. Extratropical teleconnections that cause the most prominent precipitation anomalies and extreme events over the SACZ (phases 8-1) show a similar response in EN and LN, favoring anomalous MJO convection over the CSSP, a little further east and later in EN (phases 8-1) than LN (phases 7-8). Therefore, both ENSO states provide additional forcing to produce the teleconnection, although there is a delay in the peak of the teleconnection forcing between CSSP and South American precipitation anomalies, from LN (phase 8) to EN (phase 1). The ENSO-driven modulation of regional MJO teleconnections have been the focus of many recent investigations (Arcodia et al., 2020; Ghelani et al., 2017; Henderson & Maloney, 2018; Lee et al., 2019; Moon et al., 2011; Roundy et al., 2010; Tseng et al., 2020).

Subseasonal to seasonal (S2S) predictions of the MJO and its teleconnections have improved recently (Vitart et al., 2017), but the simulation of the MJO-related teleconnections to

SA remains challenging (Grimm et al., 2021). It would be valuable to validate the ability of a model to simulate the MJO, its impacts on SA, and the modulation of those impacts by the ENSO, since the roles of ENSO and MJO on S2S predictability for South American rainfall remain unclear (Klingaman et al., 2020). The ENSO-driven modulation of the MJO teleconnections to SA is critical to S2S predictions because both phenomena are considered "windows of opportunity" for extended S2S predictability (Vitart et al., 2015). However, Klingaman et al. (2020) found no improvement in S2S predictions of South American precipitation during active ENSO and MJO periods, potentially because of short-range errors (in weeks 1-3) in MJO and ENSO teleconnections to SA (Grimm et al., 2021).

The main MJO characteristics (e.g., convection, eastward propagation) typically improve in ocean-atmosphere Coupled Global Climate Models (CGCMs) with respect to their counterpart atmosphere-only Global Climate Models (AGCMs), although the mechanisms behind the differences remain unclear (DeMott et al., 2015). MJO characteristics have improved in recent generations of CGCMs (CMIP6; Ahn et al., 2020) compared to previous generations (CMIP5; Ahn et al., 2017), but substantial deficiencies remain in amplitude and propagation. Missing or incorrect convective physics and errors in the climatological state are the primary sources for these errors. Missing convective physics affects the interaction between convection and circulation and the spatial structure of MJO diabatic heating (Jiang et al., 2015; Klingaman et al., 2015); Errors in the climatological state affect the tropical horizontal moisture distribution (Kim et al., 2017; Klingaman & Woolnough, 2014a) and also the mean circulation and atmospheric structure that change the spatial structure of convection.

Besides predicting MJO events, the ability to predict the MJO impact on the global circulation is crucial to S2S predictions (Vitart et al., 2017). The MJO extratropical teleconnections, seen as sources of the S2S predictability, improve in Global Climate Models (GCMs) that better depict the mean background flow and the MJO structure (Henderson et al., 2017). However, model physics changes that improve the MJO generally worsen the basic state (Bush et al., 2015; Kim et al., 2011; Klingaman & Woolnough 2014a).

Wang et al. (2020a) developed MJO teleconnection diagnostics to evaluate GCM biases in the Pacific North American teleconnection, while Wang et al. (2020b) described how those biases relate to the model basic state and MJO characteristics. MJO extratropical teleconnections

in the Southern Hemisphere and their behavior in GCMs have been less explored. For instance, the main MJO effect on Australian rainfall does not occur through extratropical teleconnections but through tropical teleconnections (Wheeler et al., 2009). Over SA, S2S predictions of monsoon active and break phases are hampered by incorrect reproduction of the important extratropical teleconnection from CSSP to SA (Grimm et al., 2021).

This study evaluates whether the latest atmosphere-mixed-layer-ocean coupled configuration of the Met Office Unified Model (MetUM) (Walters et al., 2019), the Met Office Global Ocean Mixed Layer (MetUM-GOML3; Giddings et al., 2020; Hirons et al., 2015; Peatman & Klingaman, 2018), reproduces the main MJO aspects, such as its activity in the Real-time Multivariate MJO (RMM) phase space, eastward propagation, convection, and teleconnections to South American rainfall. Also, we verify how the ENSO affects simulated MJO characteristics and modulates the MJO impacts over SA. Given the limited sample of observed ENSO events, it is crucial to use an extended sample of simulated ENSO events to verify recent observation-based results that show how ENSO-driven changes in the background state influence the MJO teleconnections to SA (Fernandes & Grimm, 2023).

Furthermore, we identify which aspects of the MJO and its impacts are sensitive to atmospheric horizontal resolution. Increasing horizontal resolution in previous MetUM coupled configurations improved South American precipitation and circulation patterns, especially in the SACZ (Souza Custodio et al., 2012, 2017), a region strongly affected by the MJO and ENSO (Barreiro et al., 2002; Carvalho et al., 2004; Cunningham & Cavalcanti, 2006; Alvarez et al., 2015; Hirata & Grimm, 2015; Barreiro et al., 2018; Grimm, 2019; Martín-Gomes & Barreiro, 2020; Grimm et al., 2021; Diaz et al., 2022). The MJO impact on tropical South American precipitation did not improve in the higher resolution of the latest atmospheric MetUM version (Monerie et al., 2020). Also, Solman and Blázquez (2019) concluded that increased horizontal resolution does not improve South American intraseasonal precipitation variability in many GCMs. However, these studies assessed precipitation anomalies in more than one season, smoothing the leading MJO impact on austral summer (DJF). The MJO impacts vary significantly in spring, summer, and autumn (Alvarez et al., 2015).

Section 2 describes the model, the simulations, the datasets, and the methods used. Section 3 presents the frequency of MJO activity and decay for each MJO phase in DJF for simulations with and without ENSO. Section 4 shows the MJO global anomaly patterns and precipitation anomalies over SA in the model. Section 5 shows the MJO global anomaly patterns and the precipitation anomalies over SA in EN and LN years in the model. The summary and conclusions are presented in Section 6.

2 Methodology

2.1 Model set-up

The coupled model MetUM-GOML3 comprises the MetUM atmospheric model coupled to a simplified one-dimensional ocean model, the Multi-Column K Profile Parameterization boundary-layer model (MC-KPP, based on Large et al., 1994), via the Ocean Atmosphere Sea Ice Soil (OASIS) coupler (Craig et al., 2017). One MC-KPP column is placed under each atmospheric gridpoint. MC-KPP has a 1000 m vertical domain with 100 unevenly spaced points, with the highest vertical resolution near the surface (~1 m) increasing to 25 m below 300 m.

As MC-KPP simulates only vertical mixing, temperature and salinity corrections are required in climate-length simulations to account for missing ocean dynamics and to adjust for biases in atmospheric surface fluxes (Hirons et al., 2015). The flux-correction technique constrains the mean seasonal cycle of temperature and salinity throughout the ocean column, without damping variability. The corrections are applied throughout each coupled ocean column and at each time step. The corrections are computed from an initial "tendency simulation" in which the MetUM-GOML3 is relaxed towards the target ocean climatology, with a timescale of 15 days. A relaxation timescale of 15 days is an acceptable balance between minimizing biases in the relaxation simulation and allowing the model to develop its own atmosphere-ocean coupled state. We use the 1980-2009 climatology from the Met Office (UKMO) ocean analysis (Smith & Murphy, 2007), with the addition of a repeating ENSO cycle in some simulations (see Subsection 2.2). The daily climatology of temperature and salinity corrections is computed from the output of this "tendency simulation", smoothed with a 31-day running mean to remove high-frequency variability, and applied in a subsequent "free simulation" to constrain the basic state temperature and salinity. The free simulation has no relaxation and can be integrated effectively infinitely without drift. We analyse the output of these free simulations.

177 MetUM-GOML3 differs from MetUM-GOML1 (Hirons et al., 2015) and MetUM-
178 GOML2 (Peatman & Klingaman, 2018) only by the atmospheric GCM: MetUM-GOML3 uses
179 the MetUM Global Atmosphere 7.0 (GA7; Walters et al., 2019), whereas MetUM-GOML1 uses
180 Global Atmosphere 3.0 and MetUM-GOML2 uses Global Atmosphere 6.0. GA7 has 85 levels in
181 the vertical and a model lid at 85 km. Further details on MetUM-GOML3 can be found in Hirons
182 et al. (2015) and Peatman and Klingaman (2018).

183 2.2 Simulations

184 Simulations are performed at two horizontal resolutions: 1.875° x 1.25°, the lower
185 resolution (called N96 in MetUM), with 200 km spacing between each longitude at the equator;
186 and 0.83° x 0.56°, the higher resolution (called N216), with 90 km spacing between each
187 longitude at the equator. A control MetUM-GOML3 simulation is performed at each resolution,
188 with MC-KPP constrained to the 1980-2009 ocean climatology: 30 years long at N96 and 60
189 years long at N216. Although the control simulations are constrained to reproduce the mean
190 climate of the 1980-2009 period, they do not reproduce interannual variability, since MC-KPP
191 does not simulate ocean dynamics. Thus, the years in the control simulations do not represent
192 any particular year in the 1980-2009 period, and there is no effective "time period" for these
193 simulations. Temperature and salinity corrections for these control simulations are computed
194 from a 10-year tendency simulation at each resolution.

195 **Table 1.** For each simulation, the name used in the text, the grid spacing, the length of the
196 simulation, and the target ocean state to which the model is constrained.

Name	Grid	Length	Target ocean state
N96	200 km	30 years	Smith and Murphy (2007)
N216	90 km	60 years	Smith and Murphy (2007)
N96-ENSO	200 km	60 years	3-year ENSO cycle
N216-ENSO	90 km	60 years	3-year ENSO cycle

197

198 To isolate the effect of ENSO on the MJO (Section 5), ENSO cycles are imposed in
199 MetUM-GOML3 in similar experiments to those described in Klingaman and DeMott (2020).
200 We compute one-year climatologies (May-April, to mimic the "ENSO year") from the Smith and
201 Murphy (2007) dataset for neutral, EN, and LN conditions, based on terciles of the Niño 3.4
202 index in 1980-2009. These climatologies are concatenated (in order EN, LN, neutral) to form a
203 three-year composite ENSO cycle. At each resolution, we perform a 31-year tendency
204 simulation, nudging to this three-year repeating ENSO cycle, to derive ten-year climatologies
205 (May-April) of corrections for each ENSO state. Then, at each resolution we perform a 61-year
206 free simulation imposing the corrections to obtain 20 complete 3-year cycles of May-April data.
207 These free simulations are sixty years long, providing robust statistics of simulated MJO impacts
208 on SA across many ENSO events. For more information on this technique, refer to Klingaman
209 and DeMott (2020). Control simulations, without ENSO, are named "N96" and "N216" (Table
210 1). Simulations with ENSO are named "N96-ENSO" and "N216-ENSO". N96-ENSO and N216-
211 ENSO are partitioned into EN and LN composites (e.g., N96-EN), according to simulated EN
212 and LN years.

213 2.3 Datasets

214 To validate simulated precipitation, rain gauge daily precipitation data, between 1979 and
215 2009, from the Brazilian Water Agency (ANA) and other hydrometeorological institutes from
216 SA are analyzed. The data are verified to control systematic and aleatory errors. The Liebmann
217 and Allured (2005) gridded precipitation data covers the northernmost part of SA. Both
218 precipitation datasets are gridded to 1°.

219 We validate simulated outgoing longwave radiation (OLR) against the Liebmann and
220 Smith (1996) satellite-based dataset. The streamfunction is computed (Dawson, 2016) from the
221 wind output from the MetUM-GOML3 and reanalysis from the European Centre for Medium-
222 Range Weather Forecasts (ECMWF) (ERA-Interim reanalysis data, Dee et al., 2011). All
223 observed and reanalysis data are analyzed for 1979-2009. The MJO tropical and extratropical
224 teleconnections towards SA in the ERA-Interim reanalysis streamfunction data are consistent
225 with those from the NCEP/NCAR reanalysis data, assessed by Grimm (2019) and Fernandes and
226 Grimm (2023).

2.4 Methods

2.4.1 ENSO states

Observed ENSO states are classified by the first rotated mode obtained from Principal Component Analysis (PCA) applied to 1950-2009 DJF global monthly sea surface temperature (SST) anomalies (HadISST1 dataset, Rayner et al., 2003), regridded to 5°. The PCA is based on a correlation matrix; Varimax rotation is used to obtain orthogonal rotated variability modes associated with different physical processes (Wilks, 2006). Factor scores above (below) 0.75 (-0.75) define the EN (LN) state, with the remainder classified as neutral. The classification results in 8 EN, 10 LN, and 14 neutral years (Table 1 of Fernandes & Grimm, 2023).

As MetUM-GOML3 is forced with a 3-yr repeating ENSO cycle, it is straightforward to partition N96-ENSO and N216-ENSO by terciles of the DJF mean monthly 1.5-meter temperature anomalies in the Niño 3.4 region (averaged 5°S-5°N, 170°-120°W, Fig. 1). From the 60 DJF periods in the 61-year simulations (Table 1), the warmest twenty seasons are selected as EN, the coldest twenty as LN, and the remaining twenty as neutral.

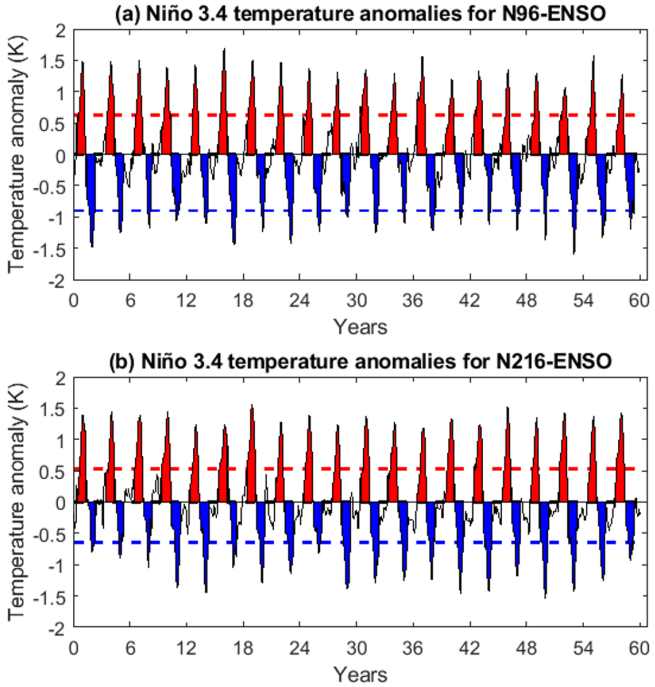

Figure 1. Timeseries of the Niño 3.4 1.5-meter temperature anomalies (°C) in (a) N96-ENSO and (b) N216-ENSO. Shading shows the May-April periods selected for the (red) EN and (blue) LN composites. The red and blue dashed lines show the thresholds for EN and LN composites, respectively. These thresholds are applied to the DJF mean index.

246 2.4.2 MJO phases

247 MJO phases are defined by the RMM indices of Wheeler and Hendon (2004). The
248 RMM1 and RMM2 indices are computed by projecting the OLR and zonal winds at 850 hPa and
249 200 hPa onto the first pair of combined empirical orthogonal functions (EOFs), computed from
250 data averaged over 15°S-15°N, after removing the mean and first three harmonics of the annual
251 cycle and the mean of the previous 120 days. As observations, we use the NOAA satellite OLR
252 data (Liebmann and Smith, 1996), and the ERA-Interim reanalysis wind data (as informed in
253 Subsection 2.3). Simulated RMM indices are computed by projecting model data onto the EOFs
254 derived from NOAA and ERA-Interim data. The MJO phases classification obtained using wind
255 data from ERA-Interim is similar to the same classification using wind data from NCEP/NCAR,
256 as Wheeler and Hendon (2004).

257 The eight MJO phases are bounded by 45° intervals of the phase angle $\theta =$
258 $\tan^{-1}\left(\frac{RMM2}{RMM1}\right)$. The MJO amplitude, for MetUM-GOML3 and observations, is defined by $A =$
259 $[(RMM1)^2 + (RMM2)^2]^{\frac{1}{2}}$. When $A \geq 1$, the MJO is active; when $A < 1$, the MJO is inactive.
260 Probabilities of MJO activity and decay (transition to the unit circle) are computed for all RMM
261 phases and each phase separately, following Klingaman and Woolnough (2014a,b).

262 2.4.3 MJO phases composites

263 Composite anomalies are calculated for each MJO phase, as in Grimm (2019), further
264 categorized according to ENSO status (EN or LN), as in Fernandes and Grimm (2023).
265 However, we have shown here composites for anomalous MJO convection and circulation only
266 for those phases with enhanced (phases 7, 8 and 1) or suppressed (phases 3 and 4) convection
267 over CSSP, the source region able to trigger the MJO extratropical teleconnections to SA. Also,
268 we display composites for anomalous MJO precipitation in simulations without ENSO only for
269 those phases with the most significant MJO impacts on South American rainfall (phases 8-5, see
270 Fig. 7 of Grimm, 2019). Composites made for periods when both ENSO and MJO are active
271 describe more efficiently the patterns than simple linear combinations of separate ENSO and
272 MJO composites (Roundy et al., 2010). Daily anomalies are computed relative to a daily
273 climatology that is smoothed with a 31-day running mean to remove spurious variance. The

anomalies are filtered (Duchon, 1979) by a 20-90 day window, using 211 weights. The filtered anomalies contain intraseasonal variability mainly related to the MJO, excluding effects from other time scales (synoptic, interannual, interdecadal), since our goal is the effect of the background ENSO-related changes on the MJO rather than the sum of the MJO and ENSO-related anomalies.

We consider only DJF anomalies because DJF is the peak of not only the monsoon over most of SA, but also the ENSO, the MJO (Hendon et al., 1999; Slingo et al., 1999), and the most substantial MJO impacts on SA (Alvarez et al., 2015; Grimm, 2019). Also, the ENSO and MJO have different rainfall responses over SA in austral spring and summer (Alvarez et al., 2015; Grimm, 2003, 2004), which argues against analyzing an extended six-month warm season. The statistical significance of the composites is assessed with the Student's *t*-test to verify whether the sample mean for each MJO phase and ENSO category in the composites is similar to the sample mean from all DJF days. The null hypothesis is rejected if the sample means are different (Wilks, 2006). As the time series are serially correlated, it is crucial to evaluate the effective sample size $n = N\left(\frac{1-\rho_1}{1+\rho_1}\right)$, in which N is the original sample size, and ρ_1 is the lag-1 autocorrelation coefficient (Wilks, 2006).

Biases and differences between the two resolutions (N216-N96) are shown in the composites presented in the Supplementary Information. The precipitation and streamfunction data are interpolated in observations and N216 onto the common coarser N96 grid; simulated OLR is interpolated onto the 2.5° grid of the observations (Liebmann & Smith, 1996). The Student's *t-test* is applied to simulated and/or observed sample means for each MJO phase to test the significance of biases.

3 MJO activity

3.1 MJO activity in N96 and N216

In both N96 and N216, the model produces strong MJO on 62% of all DJF days (Fig. 2b-c), slightly lower than the 66% observed (Fig. 2a). The MJO activity decreases to 59-61% for all days in the year in the model and 64% in observations (not shown). Klingaman and Woolnough (2014a) found a similar percentage (61%) in MetUM-GOML1. The MJO phase frequencies range between 7% and 8.5% on all days in a year in observations and in the model (see Fig. 1a-e

of Klingaman & Woolnough 2014a). However, in DJF, observed frequencies range between 4.6% (phase 1) and 13% (phase 7) (Fig. 2a).

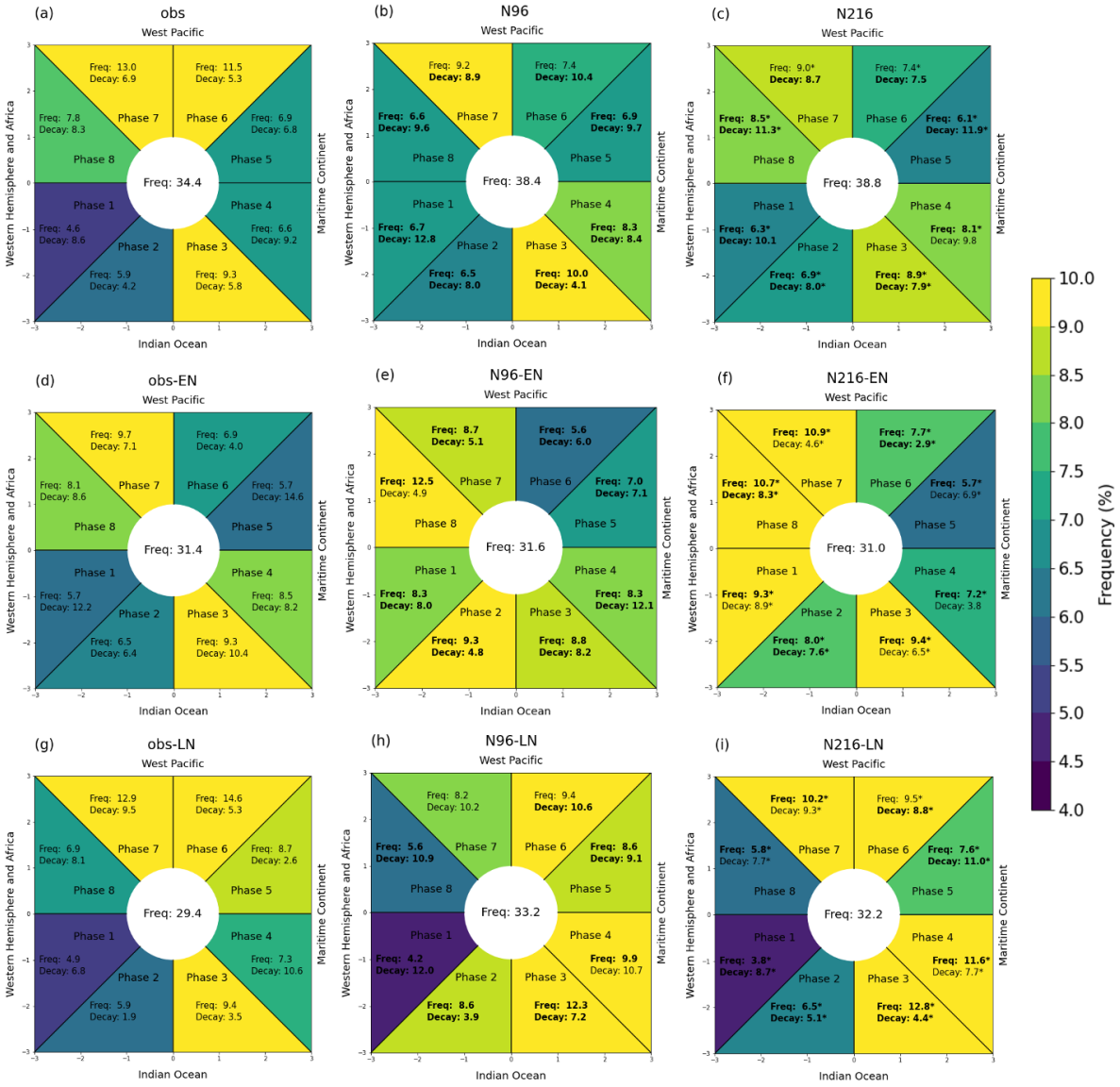

Figure 2. Percentage of MJO days in which amplitude is ≥1 (or strong MJO activity) in (a) observations (obs) (1979-2009), (b) N96, and (c) N216 during austral summer. (d-f) and (g-i) show the MJO activity like (a-c), but for N96-ENSO and N216-ENSO and only in EN year (d-f) and LN (g-i) years, respectively. The colored wedges show the daily frequency of the strong activity in each phase relative to all DJF days using the color bar. For each phase, the percentages show the probability of MJO activity in that phase ('Freq'), as well as the probability that, on the day following strong activity in that phase, the MJO moves into the unit circle ('Decay', i.e. amplitude <1). The frequency of weak MJO (amplitude <1) is given inside the unit circle. Simulated probabilities similar to those observed are in bold, and asterisks mark probabilities in N216 analogous to those in N96, considering $p < 0.05$ from a *t-test.*

316 The most frequent active MJO phases in DJF (Fig. 2a) are 7, 6, and 3, as shown by
317 Fernandes and Grimm (2023) and Grimm et al. (2021) with RMM indices from NCEP/NCAR
318 reanalysis. The less frequent active MJO phases are 1-2, followed by 4-5. This agrees with the
319 distribution of ending longitudes of tracked MJO events in Zhang and Ling (2017). The model
320 reproduces well the observed MJO frequencies in DJF, with phases 3 and 7 more frequent (9%)
321 (Fig. 2b-c), and shows decreased MJO activity in phases 1-2, though higher than observed.
322 Remarkably, the Maritime Continent barrier effect, characterized by the weakening and blocking
323 of the MJO over that region (Zhang & Ling, 2017), and therefore by a higher decay rate, which
324 in observation happens in phase 4 (Fig. 2a), is delayed to phases 5 or 6 in the model (Figs. 2b, c).
325 MJO activity is not sensitive to horizontal resolution (asterisk marks in Fig. 2c).

326 The probabilities of MJO decay and transition to the next phase (not shown) are higher in
327 the model (Fig. 2b-c) than observed (Fig. 2a). Higher transition probabilities suggest a faster
328 simulated MJO propagation than observed, which can weaken extratropical teleconnections
329 (Wang et al., 2020b). Besides, the MJO weakening as it moves from the Maritime Continent to
330 the western Pacific in the model is delayed to phases 5 or 6, with a decay is 50-100% greater in
331 the model than observed, consistent with the exaggerated Maritime Continent barrier effect in
332 CGMs (Kim et al., 2018; Vitart & Molteni, 2010). The decay in phases 5-6 in the model affects
333 the frequency of MJO phase 7 (9%), which is smaller than observed (13%), although still the
334 most frequent, along with phase 3 (9%).

335 3.2 MJO activity in each ENSO state

336 MJO frequencies conditioned on ENSO states show that active ENSO slightly increases
337 DJF MJO activity in MetUM-GOML3 and observations (Fig. 2). The frequencies slightly
338 decrease in NT years (not shown). Hence, interannual variability does not substantially affect
339 global MJO activity (Hendon et al., 1999; Slingo et al., 1999; Fernandes and Grimm, 2023).
340 However, the simulated ENSO-related anomalies affect the relative occurrence of MJO phases
341 with similar patterns of circulation anomalies as Fernandes and Grimm (2023) pointed out for
342 observations. Previous studies have shown a zonal shift of the MJO activity during ENSO over
343 the equatorial Pacific Ocean in observations and AGCMs (Fink and Speth, 1997; Hendon et al.,
344 1999; Woolnough et al., 2000; Tam & Lau, 2005; Pohl and Matthews, 2007; Wei and Ren, 2019;
345 Suematsu and Miura, 2022).

There are similarities between EN/LN states and specific MJO phases concerning the strongest anomalies of Walker circulation over the equatorial eastern Indian Ocean-western Pacific and the central Pacific. For instance, phases 8-2 (5-6) are more (less) frequent in observations in EN (Fig. 2d), compared to all years (Fig. 2a), due to enhanced (suppressed) convection over the equatorial central Pacific (eastern Indian Ocean, Maritime Continent-western Pacific). On the other hand, phases 4-6 (8-2) are more (less) frequent in LN (Fig. 2g), as the convective patterns are opposite to those described in EN (Fernandes and Grimm, 2003). This tendency is followed, on average, by the model (compare Fig. 2d to Fig. 2e-f for EN, and Fig. 2g to Fig. 2h-i for LN), although phases 8-2 are more frequent than observations in EN because in MetUM-GOML3 more EN events exceed ±0.8°C in the equatorial central-eastern Pacific (Fig. 1), favoring increased evaporation and moist static energy to enhance MJO convection.

Simulated frequencies for all MJO phases during EN are similar to those observed (bold numbers in Fig. 2e-f). Also, decay probabilities are smaller in EN (Fig. 2e-f), indicating that the EN state improves simulated eastward propagation. For example, decay probabilities in phases 5-6 are lower for EN than LN (Fig. 2h-i) and simulations without ENSO (Fig. 2b-c), suggesting that simulated MJO events in EN are more likely to move east in the western Pacific after the Maritime Continent, until they reach colder SSTs. Klingaman and DeMott (2020) found the EN state greatly improved MJO propagation in a coupled version of the Super-Parameterized Community Atmospheric Model (SPCAM3), with the same oceanic model configuration as the MetUM-GOML3.

4 MJO and its impacts in N96 and N216

4.1 Global anomaly patterns associated with MJO

4.1.1 The simulated MJO

This section shows the global evolution of the MJO tropical convection and associated circulation and the description of the MJO impacts on SA in MetUM-GOML3 at lower (N96) and higher (N216) spatial resolutions. Grimm (2019) composites are duplicated here as observations using ERA-Interim. The main aspects discussed below are common to both horizontal resolutions. The model represents well the eastward propagation of the MJO. However, the convection is further east than observed when the MJO moves from the Indian

Ocean to the Maritime Continent (phases 3-4, Fig. 3) and Western Pacific (not shown). Differences in the eastward MJO propagation are also evident in the MJO Hovmöller diagrams (Fig. 4a-c, red dashed lines) and in the displaced streamfunction quadrupoles (Figs. 5, 6), associated with Rossby and Kelvin equatorial waves (Matsuno, 1966).

The weak simulated Indian Ocean low-level westerlies and streamfunction anomalies (phases 3-4, Figs. 3b-c and 5b-c) indicate weakened equatorial Rossby waves propagating westwards, known to slow eastward MJO propagation (Chen & Wang, 2018). On the other hand, the model simulates well the magnitude of equatorial Kelvin-wave easterly anomalies. The easterlies reduce stability east of the convective center by increasing boundary layer convergence and promoting congestus convection, leading to eastward MJO propagation through the Maritime Continent (Chen & Wang, 2018). Hence, the advanced eastward propagation of the MJO convection in the model may result from the dynamical wave feedbacks of both waves (Liu & Wang, 2017). Wave feedbacks affecting the simulated MJO propagation support the "trio-interaction theory" (see Zhang et al., 2020 and references therein), which states that moist static energy, moisture feedback, and the coupling of Kelvin and Rossby waves drive the eastward MJO propagation.

The faster eastward propagation of the MJO OLR anomalies over the Indian Ocean-western Pacific in the model is visible in the more horizontal slope of the Hovmöller diagrams, between 60°E-160°E (red dashed lines, Fig. 4a-c). On the other hand, the model satisfactorily represents the MJO activity from the RMM indices (previous section), which are primarily determined by the circulation (Straub, 2013). Hence, there is an error in the convection-circulation phase relationship, since MetUM-GOML3 displaces the convection but achieves the same RMM phase.

The OLR anomalies are weaker in the model than observations (Figs. 3, 4), a common issue in climate models (Coelho et al., 2020; Kodama et al., 2015; Liu et al., 2017). Both simulations reproduce the low-level tropical circulation quadrupole (Fig. 5b-c), with the pair of cyclonic (anticyclonic) anomalies straddling the equator west (east) of the heating zone (or maximum convection, Fig. 3b-c). The baroclinic response in the tropical quadrupole appears between low and high levels (Figs. 5b-c, 6b-c). The strongest OLR and low-level wind anomalies (Fig. 3b-c) are simulated south of the equator, consistent with the DJF MJO position.

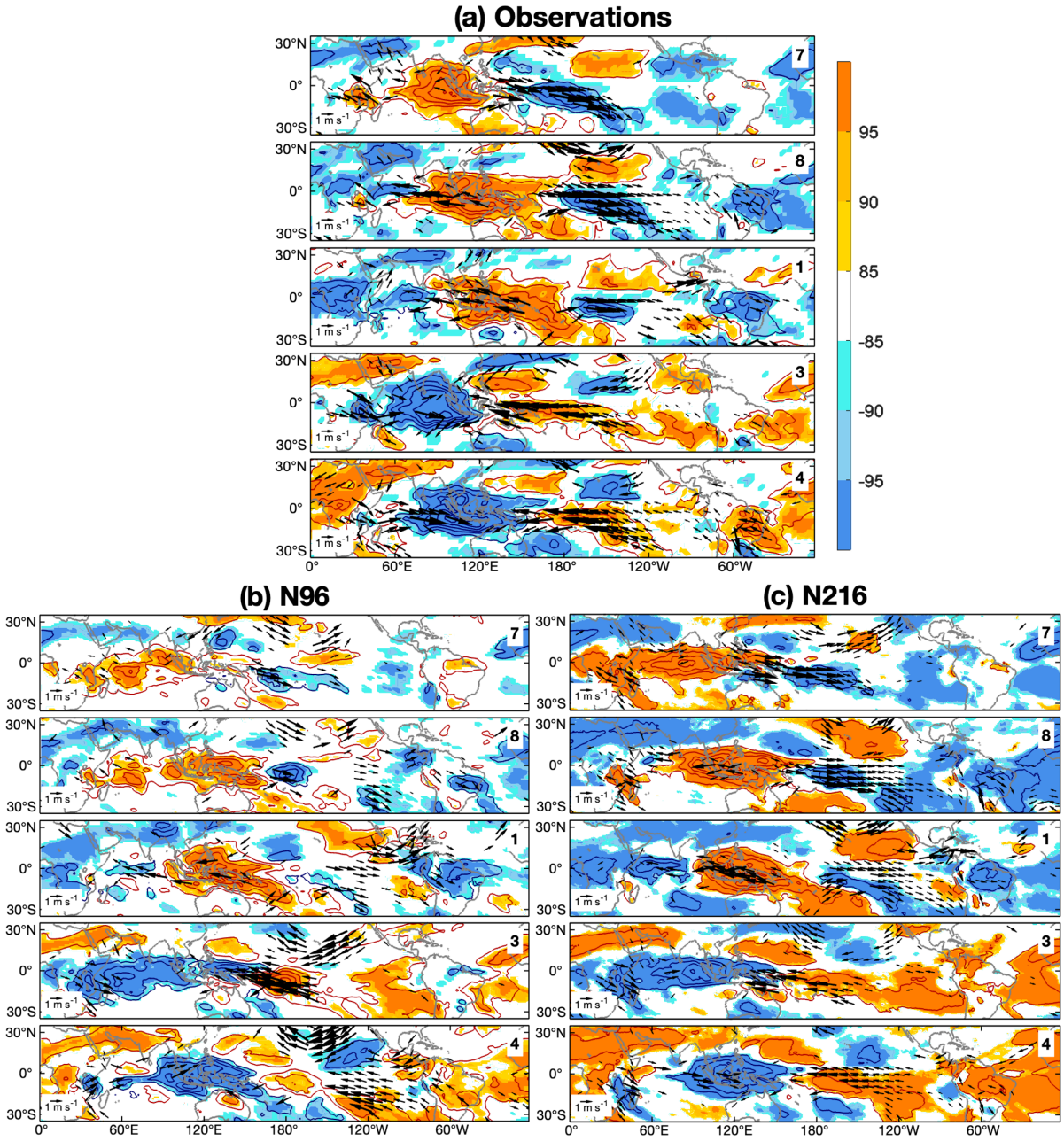

Figure 3. Composite anomalies of OLR and 850 hPa winds (black arrows) in MJO phases 7, 8, 1, 3, 4 in (a) observations, (b) N96, and (c) N216. Contour interval is 5 Wm^{-2}. The color bar indicates confidence levels, with signs indicating positive or negative OLR anomalies. Only wind anomalies (ms^{-1}) with confidence levels better than 85% are shown.

4.1.2 The simulated MJO impacts on SA through teleconnections

Focusing on the MJO impacts on SA, simulated upper-level easterlies over the central-eastern Pacific in phase 7 (Fig. 6b-c) favor the development of a significant anomalous cyclonic circulation over western tropical SA (Sakaeda & Roundy, 2016), as observed (Fig. 6a). However,

MetUM-GOML3 strengthens earlier the extratropical teleconnection between CSSP and SA (phase 8, Fig. 6b-c), associated with enhanced (suppressed) convection in the CESA (SESA) (Fig. 3b-c), than observations (Figs. 3a, 6a). While observed anomalous convection over CESA and circulation related with the teleconnection pattern are stronger in phase 1 (Figs. 3a, 6a), the simulated ones are stronger in phase 8 (Figs. 3b-c, 6b-c). The ECMWF and NCEP AGCMs also show this phase shift of the maximum extratropical teleconnection and its impacts on SA (Grimm et al., 2021). Also, the tropical teleconnection between the eastern Pacific and SA, which affects tropical precipitation anomalies, seem to reach SA earlier in MetUM-GOML3 (phase 8, Fig. 5b-c). In observations, the tropical and extratropical teleconnections to SA are fully established in phase 1 (Figs. 5a, 6a) (Grimm, 2019).

Figure 6b-c shows simulated extratropical teleconnections, indicated by curved arrows, stronger and more correctly positioned in phase 8 than 1, which differs from observations (Fig. 6a). The simulated circulation anomalies are more significant in phase 8 than 1, such as the upper-level extratropical anticyclone-subtropical cyclone pair over SA.

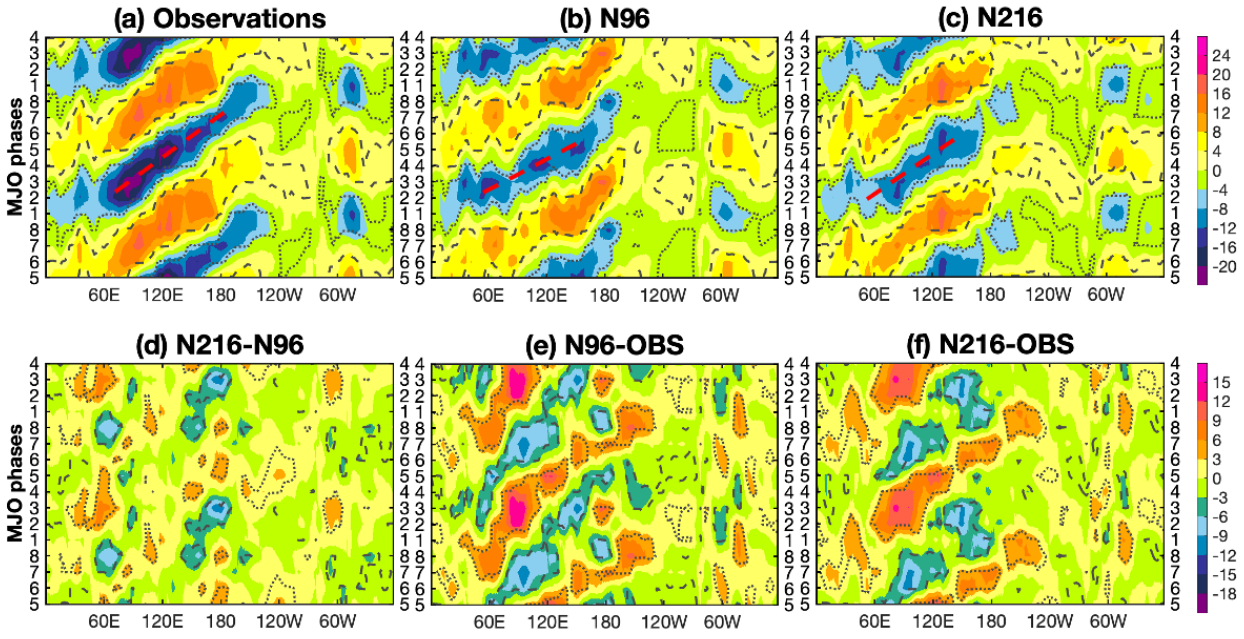

Figure 4. Time-longitude Hovmöller diagrams of 0°-15°S averaged OLR anomalies (Wm^{-2}) for (a) observations, (b) N96, (c) N216, (d) N216-N96, (e) N96-OBS, (f) N216-OBS. The dotted and dashed lines delimit positive and negative significant values with confidence levels > 85%.

435 Three main factors can shift the extratropical teleconnection to SA from phase 1 to phase
436 8 in MetUM-GOML3. (i) The eastward shift in convection for a given MJO phase with respect
437 to observations (Fig. 3a-c), which means that simulated convection arrives at the most efficient
438 source region (CSSP) "earlier" (in RMM phase space) than observed, as in Grimm et al. (2021)
439 for the ECMWF and NCEP models; (ii) the conditions over the CSSP to excite teleconnections
440 and establish the wavetrain happen almost simultaneously in the model (phase 8), whereas
441 observations show a one-phase lag between convective forcing in this region (phase 8) and the
442 teleconnection peak (phase 1) (Grimm, 2019); (iii) the simulated MJO convection (and low-level
443 convergence) over the CSSP lasts from phase 7 through 8 (Fig. 3b-c), weakening in phase 1
444 more than observed (Fig. 3a). Consequently, the extratropical teleconnections weaken in phase 1
445 (Fig. 6b-c), restricting the strongest negative OLR anomalies to equatorial North-Northeast
446 Brazil (Fig. 3b-c), where they last until phase 2 (not shown). The wavetrain fades in phase 2,
447 associated with fading anomalous convection over the CSSP and consistent with observations
448 (not shown).

449 In phase 4 (Fig. 3b-c), the model reproduces the opposite features to those in phase 8 over
450 the CSSP, associated with the phase 4 extratropical teleconnection to SA (Fig. 6b-c) (Fernandes
451 & Grimm, 2023). It is noteworthy that the model simulates the wavetrain in the expected MJO
452 phase, probably because there is no phase lag between the suppressed convection over the CSSP
453 (Fig. 3a) and the teleconnection (Fig. 6a) in observations. The simulated teleconnection favors
454 suppressed (enhanced) convection in the CESA (SESA), coherent with observations. There is an
455 upper-level extratropical cyclone-subtropical anticyclone pair over SA in MetUM-GOML3 and
456 observations, while the opposite happens in phase 8-1.

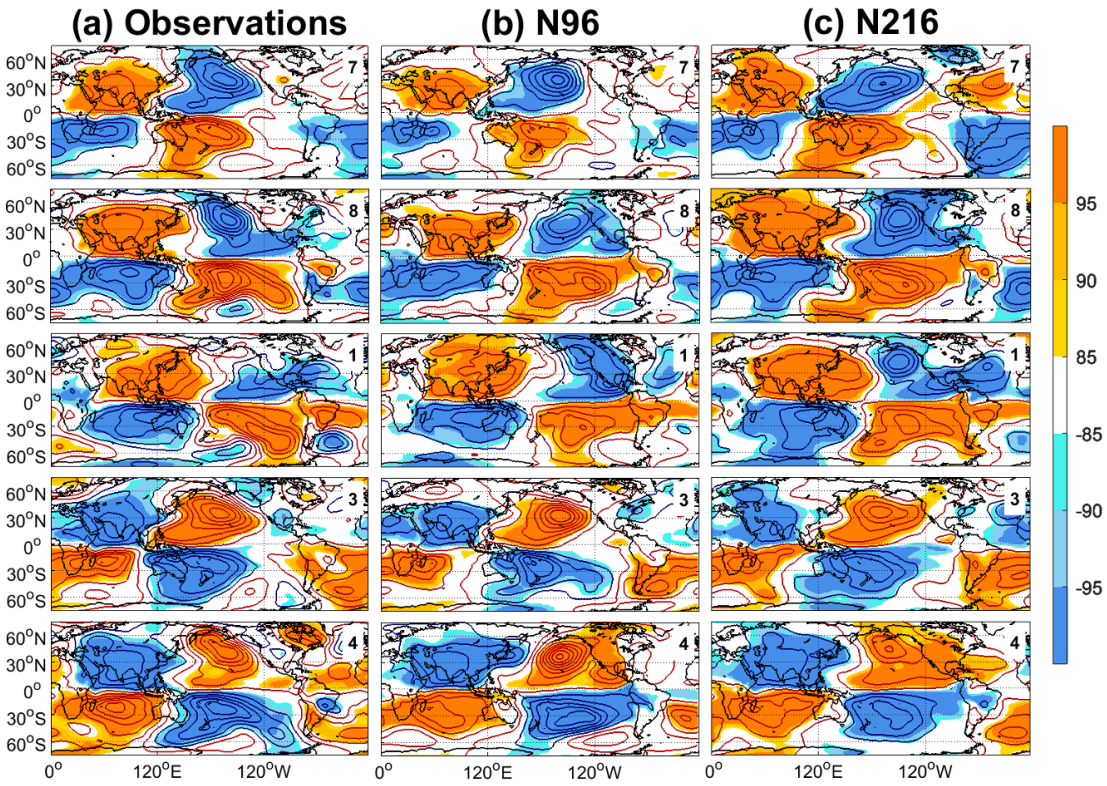

Figure 5. Composite anomalies of the 850 hPa streamfunction in MJO phases 7, 8, 1, 3, 4 in (a) observations, (b) N96, and (c) N216. Contour interval is $6 \times 10^5 m^2 s^{-1}$. Zero line is omitted. The color bar indicates confidence levels of streamfunction anomalies, with signs indicating positive or negative anomalies.

4.1.3 The effect of horizontal resolution

Despite similar overall MJO characteristics in N96 and N216 (Subsections 4.1.1 and 4.1.2), N216 improves some aspects of the MJO and its impacts on SA. Increasing resolution enhances the equatorial convection a little east of 180° (Fig. 4c-d). Also, N216 enhances convection over the CSSP for the extratropical teleconnection to SA (Grimm, 2019), better simulating the observed features in this region (phases 7-8, Figs. 3c, S1a, S1c). Significant N216-N96 differences in the negative OLR and low-level wind anomalies appear in the CSSP (phase 8, Fig. S1a).

Biases (Fig. S1b-c) show that the South American convection and low-level wind anomalies associated with the MJO are better simulated in both resolutions in phase 8 than 1. Increased horizontal resolution is important to better reproduce SESA enhanced (suppressed) convection and low-level wind anomalies in phase 4 (phase 1) (Figs. 3c, S1a). In general, the

biases in the convection anomalies over SA are smaller for N216 than for N96 (Fig. S1b-c). There are also smaller significant biases in N216 than N96 in the low-level tropical streamfunction anomalies between the eastern South Pacific and the South Atlantic (Fig. S2). Interestingly, there are more significant streamfunction biases in the extratropics than in the tropics at lower (Figs. S2b-c) and upper (not shown) levels. By contrast, there are smaller significant biases in N96 than in N216 in the upper-level streamfunction anomalies over the extratropical region (not shown), suggesting that higher resolution worsens the extratropical teleconnections. Previous studies have found an eastward displacement of the Pacific North American teleconnections due to a stronger and eastward extended North Pacific westerly jet, a common GCM bias (Henderson et al., 2017; Wang et al., 2020a, 2020b). The South American westerly jet weakens and shifts southwards in DJF. It is stronger in MetUM-GOML3 (purple contours in Fig. S3b-c) than observed (Fig. S3a), as Hirons et al. (2015) described for MetUM-GOML1.

The MJO extratropical teleconnection propagation in the model depends on the intensity of the South American westerly jet varying by the MJO phase. The jet strength differs between the lower (N96) and the higher resolution (N216) (Fig. S3b-c), as reported by previous modeling studies (Hertwig et al., 2015; Müller et al., 2018), associated with increased resolution reducing biases of the upper-level wind. Hence, N96 has a stronger westerly jet than N216 over the extratropical South Pacific and South Atlantic oceans. However, over the southern tip of SA and subtropical SA, the westerly jet is stronger in N216 (Fig. S3a,c). The southern tip of SA is the region from where the teleconnection pattern is directed towards the subtropics (Grimm, 2019).

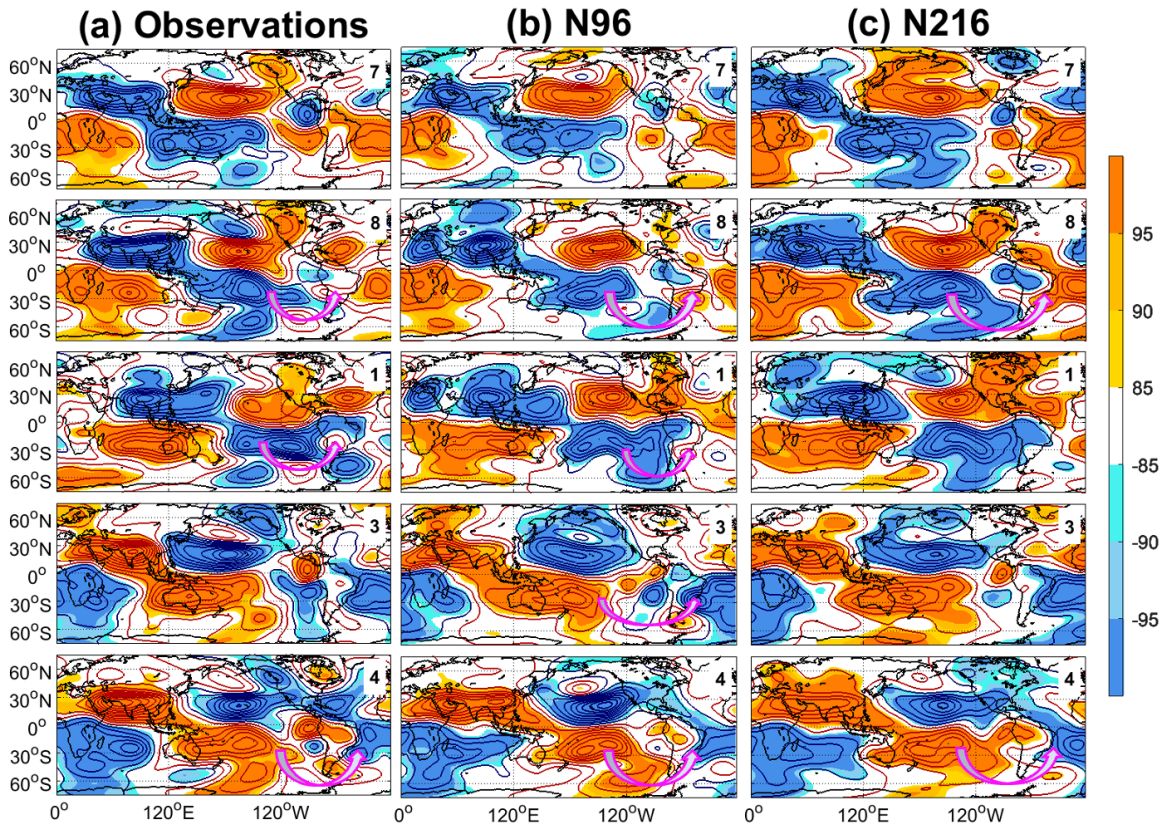

Figure 6. Composite anomalies of the 200 hPa streamfunction in MJO phases 8, 1, 3, 4 in (a) observations, (b) N96, (c) N216. Contour interval is $12 \times 10^5 m^2 s^{-1}$. The color bar indicates confidence levels of streamfunction anomalies, with signs indicating positive or negative anomalies.

Therefore, N216 may shift the extratropical teleconnection due to a stronger South American westerly jet just south of SA. Another aspect that may support the displacement of the teleconnection wavetrain is the enhanced convection over the CSSP slightly to the east in N216 with respect to N96 (phases 7-8, Fig. 3b-c). It is noticeable the teleconnections shift east at upper levels in N216 with respect to N96 (curved arrows, Fig. 6b-c). N216 shifts the upper-level anomalous circulation dipole eastwards over the subtropical South Atlantic (phases 8-1, 4, Fig. 6). In N96, the subtropical cyclonic (anticyclonic) anomaly is over or closer to SA in phases 8-1 (3-4) (Fig. 6b), consistent with observations (Fig. 6a).

4.2 Precipitation anomalies over SA associated with MJO

Figure 7 shows the CESA and SESA locations (red squares) and the precipitation anomalies over SA in MJO phases 8-5 in observations and MetUM-GOML3 simulations. The precipitation anomalies are consistent with the OLR (Figs. 3,4) and circulation (Figs. 5,6)

anomalies. The better-resolved topography in N216 improves the low-level anomalous circulation dipole in phases 8 and 4 (Fig. 5c) and the moisture flux over and around SA, indicated by the low-level wind anomalies (Fig. 3c). These features lead to an expanded anomalous precipitation dipole, in which the significant anomalies reach larger continental areas (phases 8, 1, 4, and 5, Fig. 7c). Delworth et al. (2012) and Jung et al. (2012) found mean precipitation patterns over SA improved in coupled GCMs with increased horizontal resolution. The better-resolved topography may also help the CESA mountains to anchor the SACZ in its climatological position (Grimm et al., 2007) (phase 8, Fig. 7c). The precipitation anomalies are improved in N216, even with the extratropical teleconnection to SA slightly shifted east (Fig. 6c).

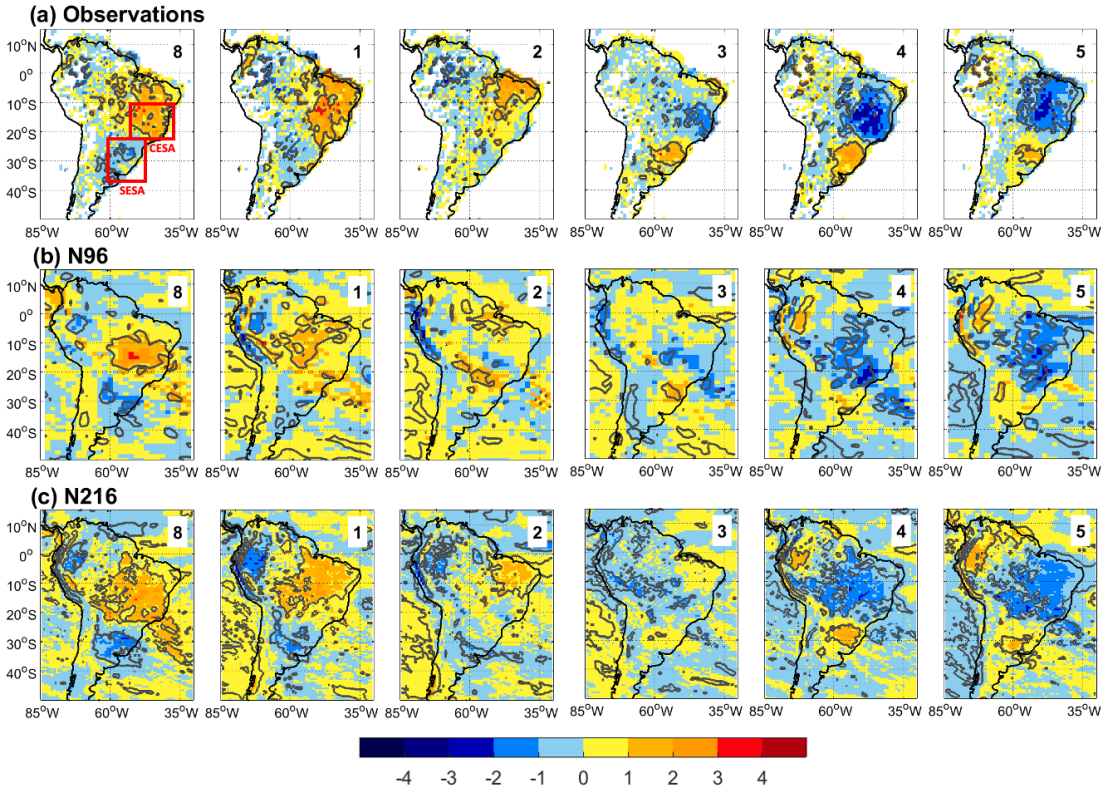

Figure 7. Composite anomalies of daily precipitation rate (color bar, $mm\,day^{-1}$), in MJO phases 8, 1, 2, 3, 4, 5 in (a) observations, (b) N96, (c) N216. Gray lines have anomalies with confidence levels better than 85%. The first map shows the CESA and SESA regions (red squares) cited in the text.

Simulated precipitation anomalies are significant over the entire CESA in phase 8, when both teleconnections are fully established (Figs. 5b-c, 6b-c). On the other hand, the anomalies are much reduced over CESA (and over the SACZ) in phase 1 (Fig. 7b-c), as the extratropical

teleconnection weakens (Fig. 6b-c). The significant positive anomalies retreat to the north of CESA and equatorial northeast (NE) Brazil in phase 1, as do the OLR anomalies (Fig. 3b-c), consistent with tropical teleconnections (Figs. 5b-c).

Positive precipitation anomalies are enhanced in N216 with respect to N96 over the Northeast Brazil in phases 1-2, and in SESA, in phases 4-5 (Fig. S4a). The precipitation dipole is shifted westward in the model (Fig. 7b-c), over the monsoon core region (10°-20°S, 45°-55°W, smaller red squares in Fig. S4b-c) and the Amazon in phases 8, 1, 4, 5. The MJO impacts are more significant in observations (Fig. 7a) in CESA, a little east of the monsoon core region (Grimm, 2019). The model overestimates the daily precipitation climatology in DJF over these regions, corroborating Souza Custodio et al. (2017), with differences larger than 3 mm/day (not shown), and favors enhanced MJO precipitation anomalies, which range between +/- 5 mm/day. On the other hand, the model underestimates the precipitation anomalies in CESA (phase 1) and in equatorial NE Brazil (phases 8-1) (Fig. S4b-c).

The most significant positive precipitation anomalies in SESA, sometimes associated with Mesoscale Convective Systems occur in phases 3-4, weakening in phase 5 (Fig. 7a). N216 represents better than N96 these anomalies during phases 4-5 (Fig. 7b-c) due to improved convection and low-level circulation anomalies (phase 4, Figs. S1, S2). Monerie et al. (2020) hypothesized that increased horizontal resolution in MetUM improved the representation of Mesoscale Convective Systems over SA.

5 MJO impacts during El Niño and La Niña states

The following subsections show the global anomalous MJO convection and circulation patterns in EN and LN in MetUM-GOML3 (Subsection 5.1) and related South American precipitation anomalies (Subsection 5.2). Fernandes and Grimm (2023) composites are duplicated here as observations using ERA-Interim.

5.1 Global anomaly patterns associated with MJO in EN and LN

5.1.1 Influence of EN and LN states on the simulated MJO

In N96-ENSO and N216-ENSO, the global MJO OLR, wind at 850 hPa (Figs. 8b-c,e-f, 9b-c,e-f), and streamfunction anomalies (Figs. 10b-c,e-f, 11b-c,e-f) strengthen (weaken) in EN (LN) with respect to N96 and N216 (Figs. 3b-c, 4b-c, 5b-c, 6b-c). Hence, it is noticeable that the

own MJO strengthens (weakens) in EN (LN). For instance, the magnitude of the low-level westerlies over Africa and Indian Ocean, associated with the drag effect of the equatorial Rossby waves (Wang et al. 2018), are closer to observations in EN (phases 3-4, Fig. 8b-c) than LN (Fig. 8e-f). Also, the low-level easterlies of equatorial Kelvin waves and the suppressed convection over the western Pacific are more significant in EN (phases 3-4, Figs. 8b-c, 9b-c) than LN (phases 3-4, Figs. 8e-f, 9e-f), supporting MJO propagation (Chen and Wang, 2018; Kim et al., 2014), as found in observations (Fernandes & Grimm, 2023) and the atmosphere-mixed-layer-ocean coupled configuration of ECHAM4 (Wei & Ren, 2019).

In addition, the OLR and U850 Hovmöller diagrams (Fig. 9a-l) show that EN conditions produce the best simulated MJO eastward propagation, in agreement with Klingaman and DeMott (2020), as well as less MJO decay, mainly over the Maritime Continent-western Pacific (Fig. 2e-f). The magnitude of the equatorial OLR and U850 anomalies is closer to observations in EN than LN (Fig. 9a-l) or simulations without ENSO (Fig. 4). We hypothesize that the simulated EN strengthens moisture gradients near the Maritime Continent, inducing more moisture advection by the stronger low-level wind anomalies during the EN state (Fig. 8b-c), favoring MJO eastward propagation through the Maritime Continent (Wei and Ren, 2019). The faster eastward propagation of the MJO convection over the Indian Ocean-Maritime Continent is visible in the lower slope of the Hovmöller diagram between 60°E-160°E (red dashed lines, Fig. 9a-f) in EN than LN. In other words, the MJO convection is further east in EN than LN from phase 3 through phase 5 (Henderson & Maloney, 2018; Wei & Ren, 2019; Fernandes & Grimm, 2023). The simulated MJO suppressed convection weakens during LN (Fig. 9e-f) over the Indian Ocean-Maritime Continent, producing a standing oscillation near the Maritime Continent. Therefore, the Maritime Continent barrier effect (Zhang & Ling, 2017), enhanced in GCMs (Kim et al., 2018; Vitart & Molteni, 2010), is even more exaggerated in LN, mainly in N96-LN (Fig. 8e, phases 3-4), consistent with the increased MJO decay in phases 5-6 in LN (Fig. 2h-i).

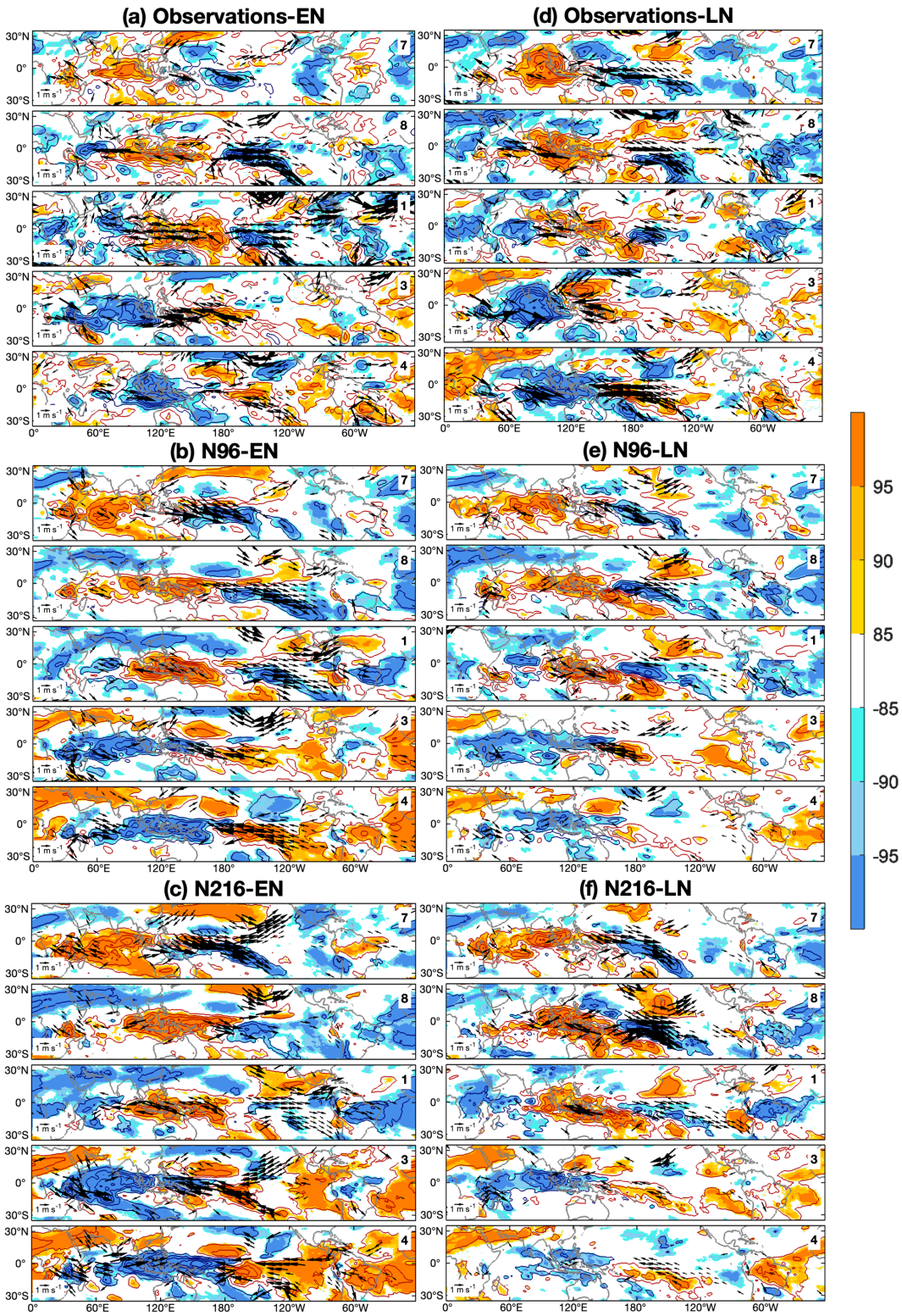

Figure 8. Same as Figure 3, but for (a) observations-EN, (b) N96-EN, (c) N216-EN, (d) observations-LN, (e) N96-LN, and (f) N216-LN.

591 Changes in the Walker circulation by ENSO affecting MJO convection are often better
592 simulated in the higher resolution. For example, the anomalous MJO and EN (LN) convection
593 with the same (opposite) signal across the central Pacific during phases 6-7 (not shown) increase
594 the subsidence and suppressed convection over the equatorial northeast SA in N216-EN (phase
595 7, Fig. 8c) and the ascent and enhanced convection over the same region in N216-LN (phase 7,
596 Fig. 8f). Thus, simulated dry anomalies over the equatorial northeast SA last longer in N216-EN
597 (phases 4-7) than N216-LN (phases 4-5) (not shown), establishing the convective dipole over SA
598 with an opposite sign later in N216-EN (phase 8) than N216-LN (phase 7) (Fig. 8c,f), consistent
599 with observations (Fig. 8a,d). The persistent dipole from phases 4-7 in EN is noticeable in the
600 precipitation anomalies (Subsection 5.2). Interestingly, anomalous convection over the equatorial
601 northeast SA in phase 8 is stronger in LN than EN in both resolutions (Fig. 8b-c,e-f), as observed
602 (Fig. 8a,d), associated with changes in the Walker circulation by EN (LN), decreasing
603 (increasing) the ascent over that region. However, the equatorial convection over SA in the
604 Hovmöller diagrams is more prominent in LN than EN, as observed (Fig. 9a,d), only in N216
605 simulations (phases 8-2, Fig. 9c,f).

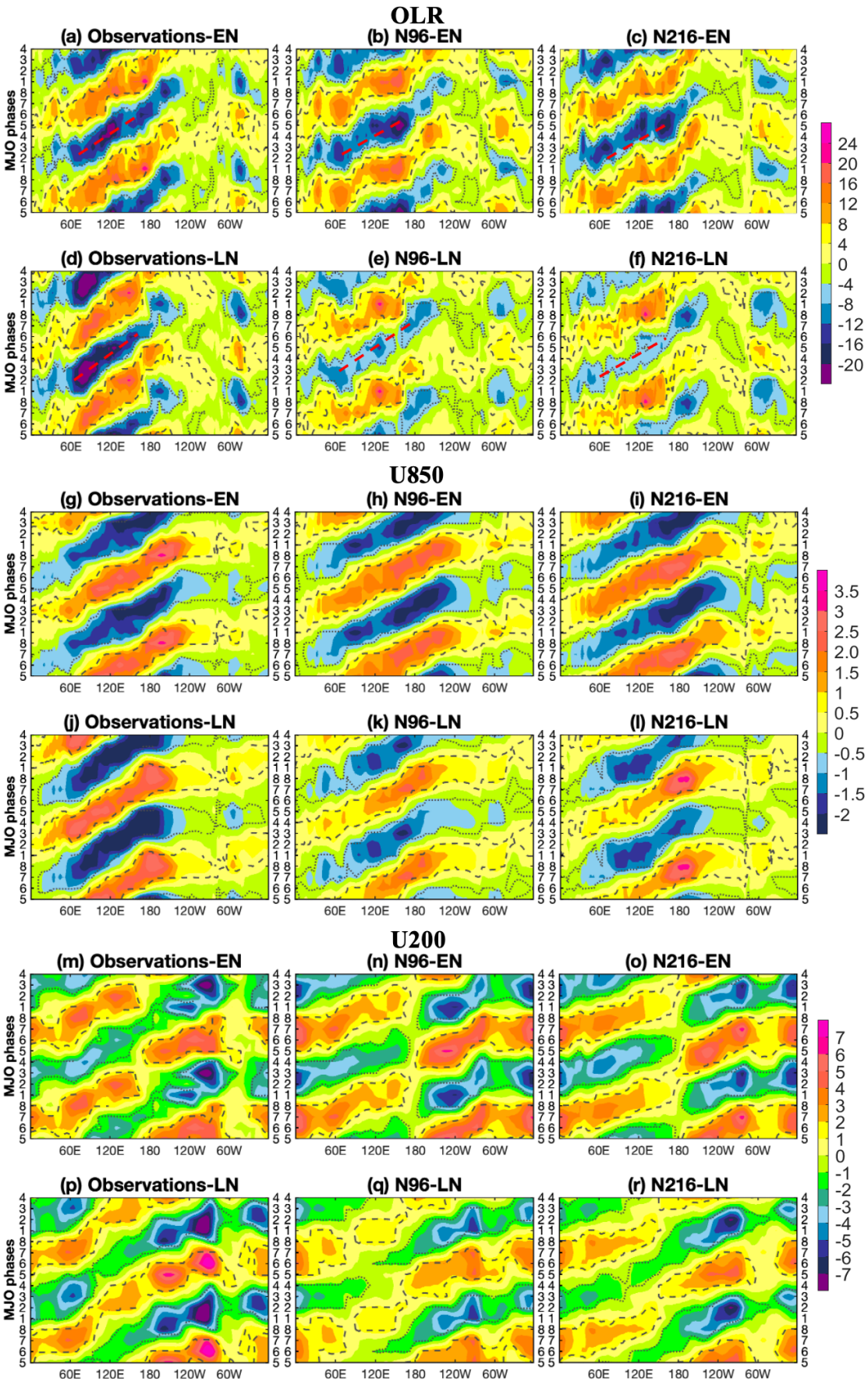
OLR
(a) Observations-EN
(b) N96-EN
(c) N216-EN
(d) Observations-LN
(e) N96-LN
(f) N216-LN
MJO phases
60E 120E 180 120W 60W
24 20 16 12 8 4 0 -4 -8 -12 -16 -20
U850
(g) Observations-EN
(h) N96-EN
(i) N216-EN
(j) Observations-LN
(k) N96-LN
(l) N216-LN
3.5 3 2.5 2.0 1.5 1 0.5 0 -0.5 -1 -1.5 -2
U200
(m) Observations-EN
(n) N96-EN
(o) N216-EN
(p) Observations-LN
(q) N96-LN
(r) N216-LN
7 6 5 4 3 2 1 0 -1 -2 -3 -4 -5 -6 -7

606

607 **Figure 9.** MJO phase-longitude Hovmöller diagrams of 0°-15°S averaged OLR anomalies
608 (Wm^{-2}), averaged zonal wind anomalies at 850 and 200 hPa (ms^{-1}), for each of the eight
609 MJO phases during the austral summer in observations-EN (a,g,m), observations-LN (d,j,p),
610 N96-EN (b,h,n), N96-LN (e,k,q), N216-EN (c,i,o), N216-LN (f,l,r). The dotted and dashed lines
611 delimit the significant values with confidence levels > 85%.
612
613 *5.1.2 Influence of EN and LN states on the MJO teleconnections and their impacts on SA*

614 The MJO convection increases over the central-eastern South Pacific in phases 7-1 in
615 both EN and LN states (Fig. 8a,d), strengthening the extratropical teleconnection (Fig. 11a,d)
616 that produces more rainfall in CESA, especially in its southern part (Fernandes & Grimm, 2023;
617 Grimm, 2019). Enhanced low-level convergence (Fig. 8a,d) and upper-level easterlies (Fig.
618 11a,d) favor the maximized MJO convection. The MJO convection over the CSSP in phases 8-1
619 is more significant in N96-EN (Fig. 8b) than N216-EN (Fig. 8c) and simulations without ENSO
620 (Fig. 3b-c), supported by increased low-level convergence (Fig. 8b) and upper-level easterlies
621 (Fig. 11b). We hypothesize that the anomalous equatorial convection extended further east of
622 180° in N96-EN (Fig. 9b) than N216-EN (Fig. 9c) increases the probability of enhanced
623 convection over the CSSP to efficiently trigger the teleconnections towards SA in phases 8-1. In
624 LN, the MJO convection is shifted westward to the subtropical South Pacific in phases 7-8 in
625 both resolutions (Fig. 8e,f) as in observations (Fig. 8d) (Fernandes & Grimm, 2023; Moon et al.,
626 2011), coherent with colder equatorial SST and enhanced subsidence east of 180°, and the
627 convection is stronger than simulations without ENSO (Fig 3b-c).

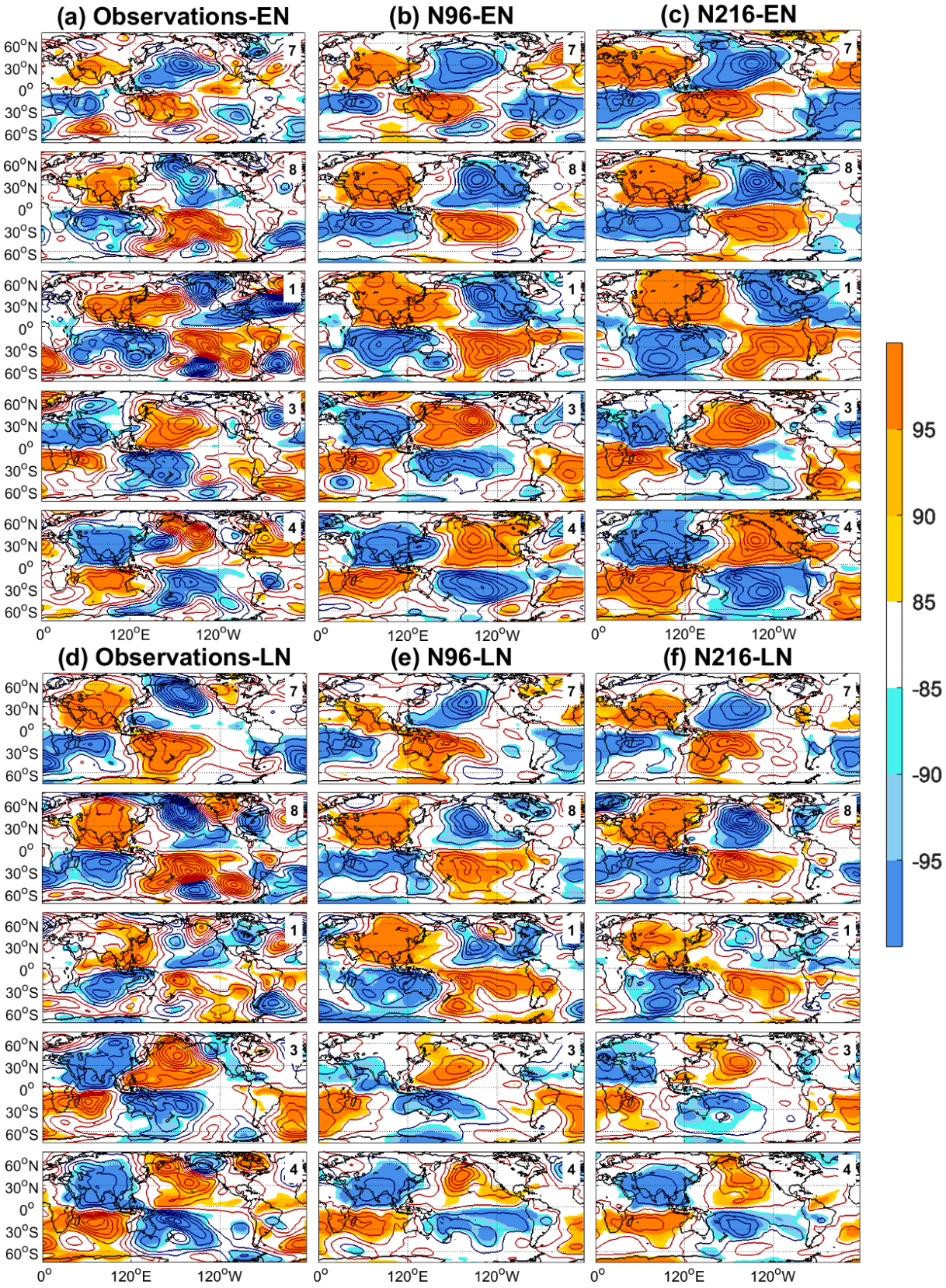
(a) Observations-EN
(b) N96-EN
(c) N216-EN
(d) Observations-LN
(e) N96-LN
(f) N216-LN
60°N
30°N
0°
30°S
60°S
0°
120°E
120°W
7
8
1
3
4
95
90
85
-85
-90
-95

628

Figure 10. Same as Figure 5, but for (a) observations-EN, (b) N96-EN, (c) N216-EN, (d) observations-LN, (e) N96-LN, and (f) N216-LN.

Notwithstanding, enhanced MJO convection strengthens in N96-EN (phases 8-1, Fig. 8b) and N216-LN (phases 7-8, Fig. 8f) over the CSSP, supported by low-level convergence. In N216-EN, the anomalies weaken too early in phase 8 (Fig. 8c) and in N96-LN, they are too far west with respect to the CSSP location (Fig. 8e). Consequently, extratropical teleconnections (pink curved arrows in Fig. 11) are best simulated in N96-EN (phase 8, Fig. 11b) and N216-LN (phases 8-1, Fig. 11f) but also visible in N96-LN (phase 8, Fig. 11e). N96-EN also shows increased subtropical temperature latitudinal gradient between the equatorial eastern Pacific and the CSSP with respect to N216-EN (not shown), which favors a stronger subtropical jet supporting the propagation and establishment of the MJO teleconnection wavetrain.

The model teleconnection pattern is already fully established in phase 8, even with N96-EN simulating enhanced conditions over the CSSP in phase 1 (Fig. 8b). By contrast, observations-EN shows the teleconnection wavetrain peaking in phase 1 (Fig. 11a), related to the convection and low-level convergence still strong in phase 1 (Fig. 8a). Hence, adding ENSO did not change the issue in the model in simulating the peak of the teleconnection pattern earlier (phase 8) than observed (phase 1) because the simulated MJO is still propagating faster and the teleconnection pattern peaks simultaneously with enhanced conditions over the CSSP in the model. Notable component of the MJO teleconnection pattern is the upper-level anomalous circulation dipole over subtropical and extratropical SA. The extratropical anomalous barotropic anticyclonic circulation in phases 8-1 is shifted west in the model in phase 8 (Figs. 10 and 11), and weakens in phase 1 due to the decay of the teleconnection pattern. However, it is still visible in N216-LN at both levels (Figs. 10f, 11f). The simulated upper-level cyclonic anomaly associated with enhanced rainfall in the SACZ is stronger in phase 8 than 1 (Fig. 11b,e,f).

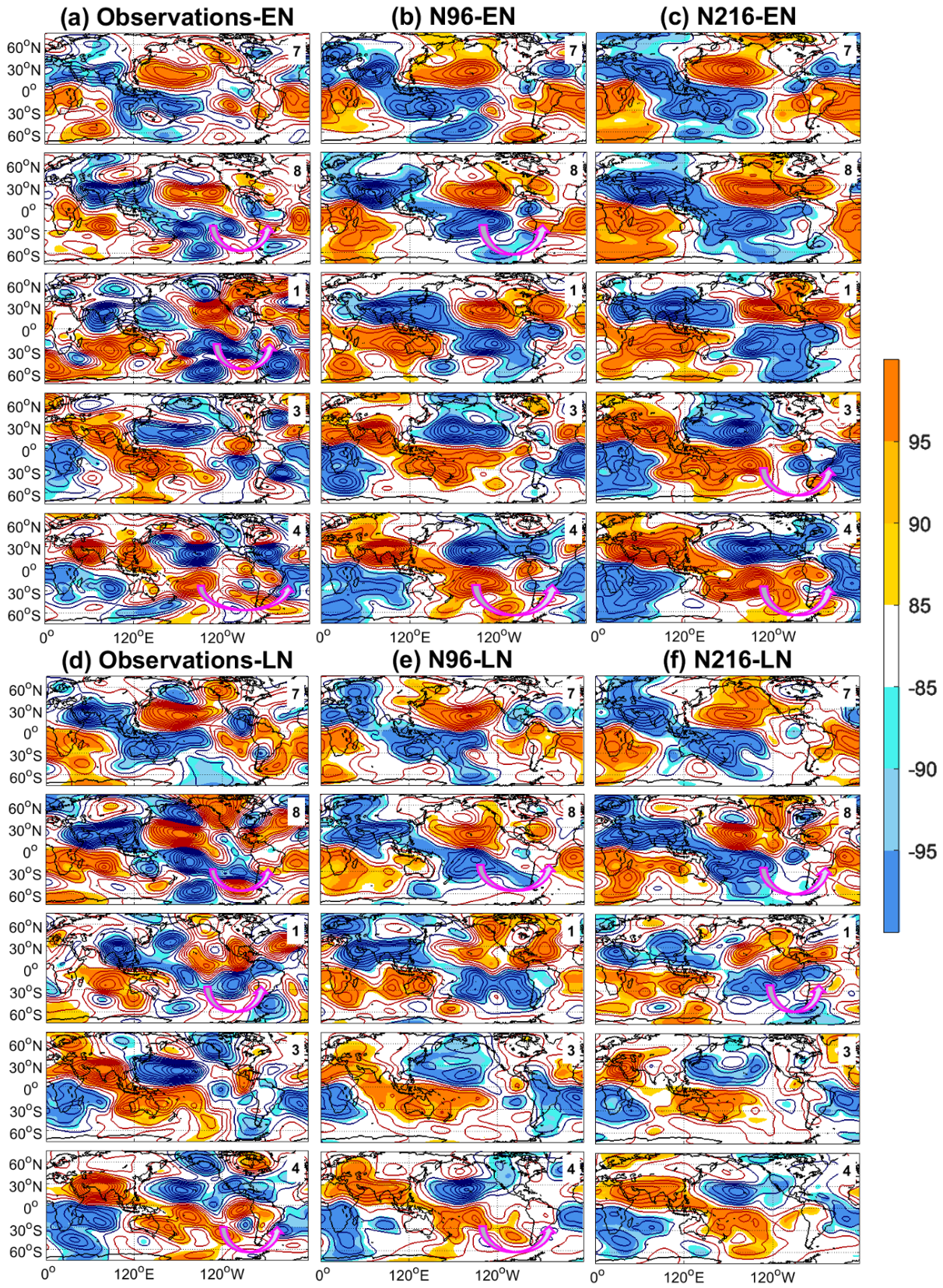
(a) Observations-EN
(b) N96-EN
(c) N216-EN
(d) Observations-LN
(e) N96-LN
(f) N216-LN
60°N
30°N
0°
30°S
60°S
0°
120°E
120°W
7
8
1
3
4
95
90
85
-85
-90
-95

654

655 **Figure 11.** Same as Figure 6, but for (a) observations-EN, (b) N96-EN, (c) N216-EN, (d)
656 observations-LN, (e) N96-LN, and (f) N216-LN.
657
658 Equatorial suppressed MJO convection east of 180° in phases 3-4 is stronger in EN and
659 LN (Fig. 9a,d) than in all years (Fig. 4a). The suppressed convection starts to shift
660 southeastwards, entering into the favorable region to excite the phase 4 extratropical
661 teleconnection pattern to SA (Fernandes & Grimm, 2023), which produces positive (negative)
662 OLR anomalies in CESA (SESA) (Subsection 4.1). In the model, the equatorial suppressed
663 convection extends east of 180° only in EN (Fig. 9b-c), because the Maritime Continent barrier
664 effect magnifies in LN (Fig. 9e-f). N96-EN (phase 4) and N216-EN (phases 3-4) show
665 maximized suppressed convection supported by enhanced low-level divergence over the CSSP
666 (Fig. 8b-c), able to trigger stronger extratropical teleconnections (Fig. 11b-c) than in simulations
667 without ENSO (Fig. 6b-c). The teleconnection pattern is shifted east in N216-EN with respect to
668 N96-EN, as simulations without ENSO. However, the wavetrain in N216-EN is more accurately
669 positioned, as the anomalous circulation dipole is adjacent to the South American continent,
670 coherent with observations-EN (Fig. 11a).

671 The conditions over the CSSP to excite the wavetrain weaken in LN in the model (phases
672 3-4, Fig. 8e-f), and a weaker teleconnection pattern is visible in N96-LN (phase 4, Fig. 11e). In
673 observations, the enhanced (suppressed) convection is stronger and further east in EN (LN) than
674 LN (EN) over the CSSP in phases 8-1 (3-4), so the teleconnection pattern and its impacts on SA
675 are shifted east in EN (LN) with respect to LN (EN) in phase 1 (phase 4) (Fig. 11a,d) (Fernandes
676 & Grimm, 2023). This shift also happens in the model in phases 1 and 4 (cf Figs. 11b-c,11e-f).

677 The eastward MJO propagation over the central-eastern Pacific slows (quickens) in EN
678 (LN) due to warmer (colder) SSTs and stronger (weaker) convection during phases 6-7 (Zhang,
679 2005), establishing the tropical teleconnection towards SA earlier in LN (phase 8, Fig. 10d) than
680 EN (phase 1, Fig. 10a) (Fernandes & Grimm, 2023). This difference in the eastward MJO
681 propagation between EN and LN is more clearly visible in the U200 Hovmöller diagrams (Fig.
682 9m,p). The equatorial upper-level zonal winds best represent the eastward MJO propagation over
683 colder SSTs in the equatorial central-eastern Pacific than the equatorial OLR and low-level zonal
684 winds (Fig. 9). In observations, LN (Fig. 9p) displays stronger upper-level zonal winds and lower
685 slopes than EN (Fig. 9m) (Fernandes & Grimm, 2023).

686 In MetUM-GOML3, EN (Fig. 9n-o) and LN (Fig. 9q-r) show similar magnitude and
687 propagation of the equatorial upper-level zonal winds over the equatorial central-eastern Pacific.
688 As the model lacks ocean dynamics, it does not simulate well changes in the upwelling in the
689 eastern part of the oceans in response to changes in the trade winds. Changes in the thermocline
690 depth and SST related to ENSO are controlled by temperature and salinity corrections imposed
691 in MetUM-GOML3. Hence, the strength of the Walker circulation over the "deficient" upwelling
692 region in the equatorial eastern Pacific is not well simulated and the upper-level zonal winds are
693 different from those in observations. Nonetheless, the model reproduces changes in the MJO
694 eastward propagation due to differences in ENSO SST and convection anomalies over the
695 Maritime Continent-western Pacific (Subsection 5.1.1), and also over the central-eastern Pacific,
696 delaying the peak of the tropical teleconnection to SA in EN (phase 1) with respect to LN (phase
697 8) (Fig. 10b-c,e-f).

698 5.2 Precipitation anomalies over SA associated with MJO in EN and LN

699 Figures 12 and 13 show the simulated precipitation anomalies over SA in each MJO
700 phase in EN and LN states. A transition from negative to positive (positive to negative)
701 precipitation anomalies over CESA (SESA) starts in phase 7, reaching the strongest precipitation
702 anomalies in phase 1 (Fig. 7 of Grimm, 2019). The model follows approximately this evolution
703 (not shown), consistent with observations, but peaking the South American precipitation
704 anomalies one phase earlier (phase 8) (Fig. 7). During LN (Fig. 13a), the evolution is a little
705 advanced in relation to EN (Fig. 12a), as the transition that in EN starts in phase 7, in LN is
706 almost completed in this phase, and the maximum precipitation anomalies in CESA happen in
707 phase 8. The model reproduces this difference (Figs. 12b-c,13b-c), and also the stronger positive
708 anomalies over NE Brazil in phase 2 during LN.

709 MJO circulation anomalies differ over the continent between N96-EN and N216-EN in
710 phase 8 (Fig. 11b-c). The strong extratropical anticyclone-subtropical cyclone pair over SA,
711 linked to the extratropical teleconnection, appears well defined only in N96-EN. Hence,
712 significant positive SACZ precipitation anomalies in southern CESA appear in N96-EN (Fig.
713 12b) during phase 8. In N216-EN and phases 8-1, the precipitation anomalies shift to northern
714 CESA (Fig. 12c). Both resolutions reproduce the enhanced positive precipitation anomalies in
715 tropical CESA and NE Brazil during phase 1 in EN (Fig. 12b-c), supported by strong low-level

westerly wind anomalies (Fig. 8b-c), associated with the fully established tropical teleconnection (Fig. 10b-c), coherent with observations-EN (Figs. 8a, 10a, 12a).

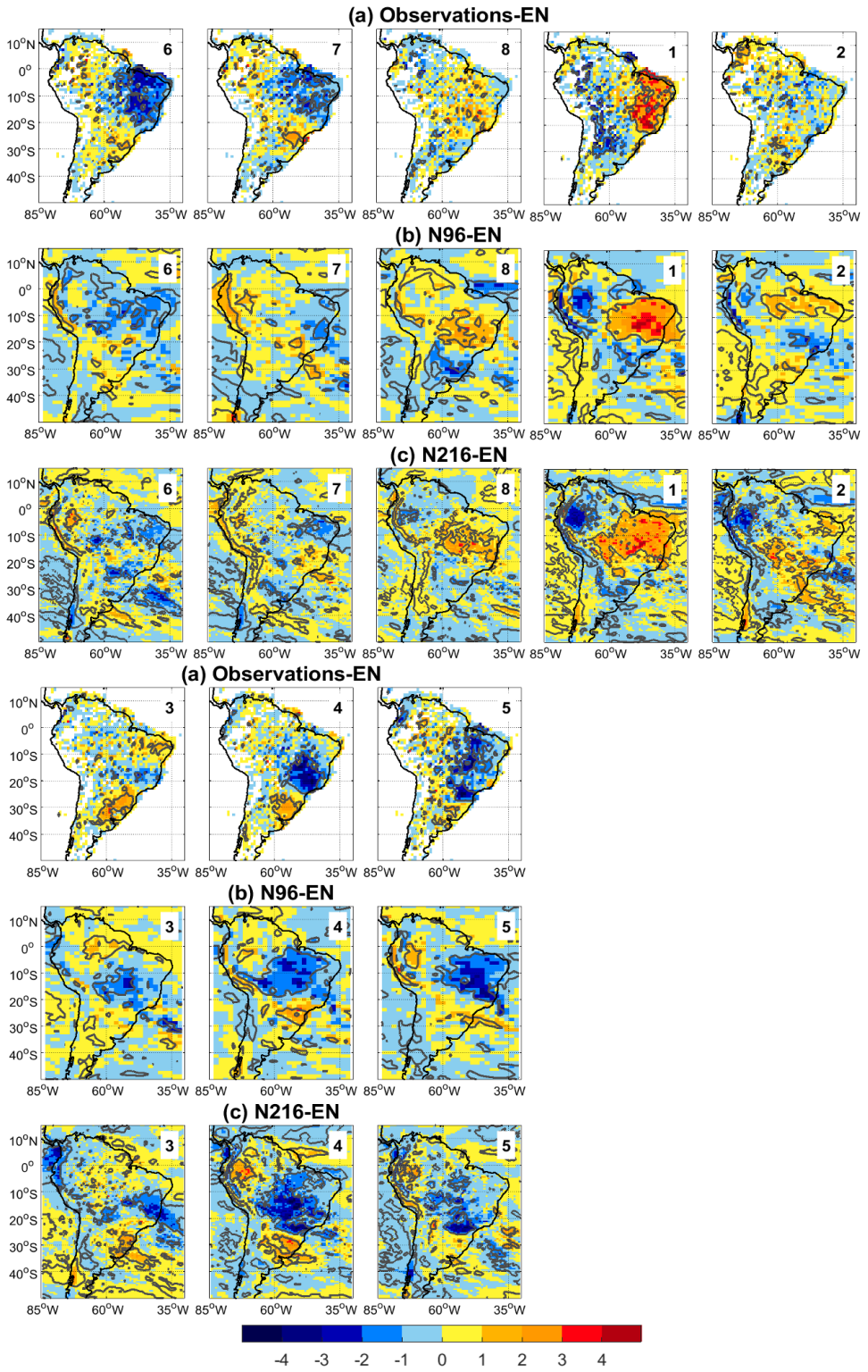

Figure 12. Same as Figure 7, but for (a) observations-EN, (b) N96-EN, and (c) N216-EN.

720 Simulations under the LN state show the most prominent anomalous precipitation dipole
721 in phase 8 (Fig. 13b-c), consistent with observations-LN (Fig. 13a). The equatorial waves
722 strengthen positive precipitation anomalies from tropical CESA to NE Brazil. The extratropical
723 Rossby wavetrain intensifies the subtropical precipitation anomalies and its circulation dipole
724 over SA favors low-level moisture flux from the Amazon, increasing SACZ precipitation. The
725 precipitation dipole is even better in N216-LN, as a result of the improvement in simulating the
726 extratropical anticyclone-subtropical cyclone pair over SA (Fig. 11f). Thus, the nonlinear ENSO
727 effect on the most significant precipitation anomalies in the SACZ through extratropical
728 teleconnections happens in phase 8 in the model (Figs. 12b, 13b-c), as the wavetrain decays in
729 phase 1 (Fig 11b,e,f). In observations, the nonlinear ENSO effect starts in phase 8 and peaks in
730 phase 1 (Figs. 12a, 13a).

731 Increased horizontal resolution improves precipitation anomalies in LN, bringing the
732 model closer to observations-LN in phase 8. For instance, significant positive precipitation
733 anomalies extend over the eastern Amazon and NE Brazil in N216-LN in phases 8-2 (Fig. 13c),
734 consistent with enhanced convection over northeastern SA in N216-LN (Fig. 8f, phase 2 not
735 shown). Also, negative precipitation anomalies appear in SESA in N216-LN in phases 7-1,
736 enhanced by LN-driven subsidence added to the MJO effect (Grimm, 2004, 2019).

737 A transition from positive to negative (negative to positive) precipitation anomalies over
738 CESA (SESA) starts in phase 3 (Fig. 7a). The anomalous precipitation dipole in phases 3-4 in
739 N216-EN (Fig. 12c) is coherent with observations-EN (Fig. 12a), shifted southeast with respect
740 to N96-EN (Fig. 12b), as a response to the improved extratropical teleconnection (Fig. 11c). In
741 EN, the positive precipitation anomalies in the southern part of SESA last from phases 3 to 7 in
742 both resolutions, consistent with observations-EN and the EN effect on SESA added to the MJO
743 effect (Grimm, 2003, 2019).

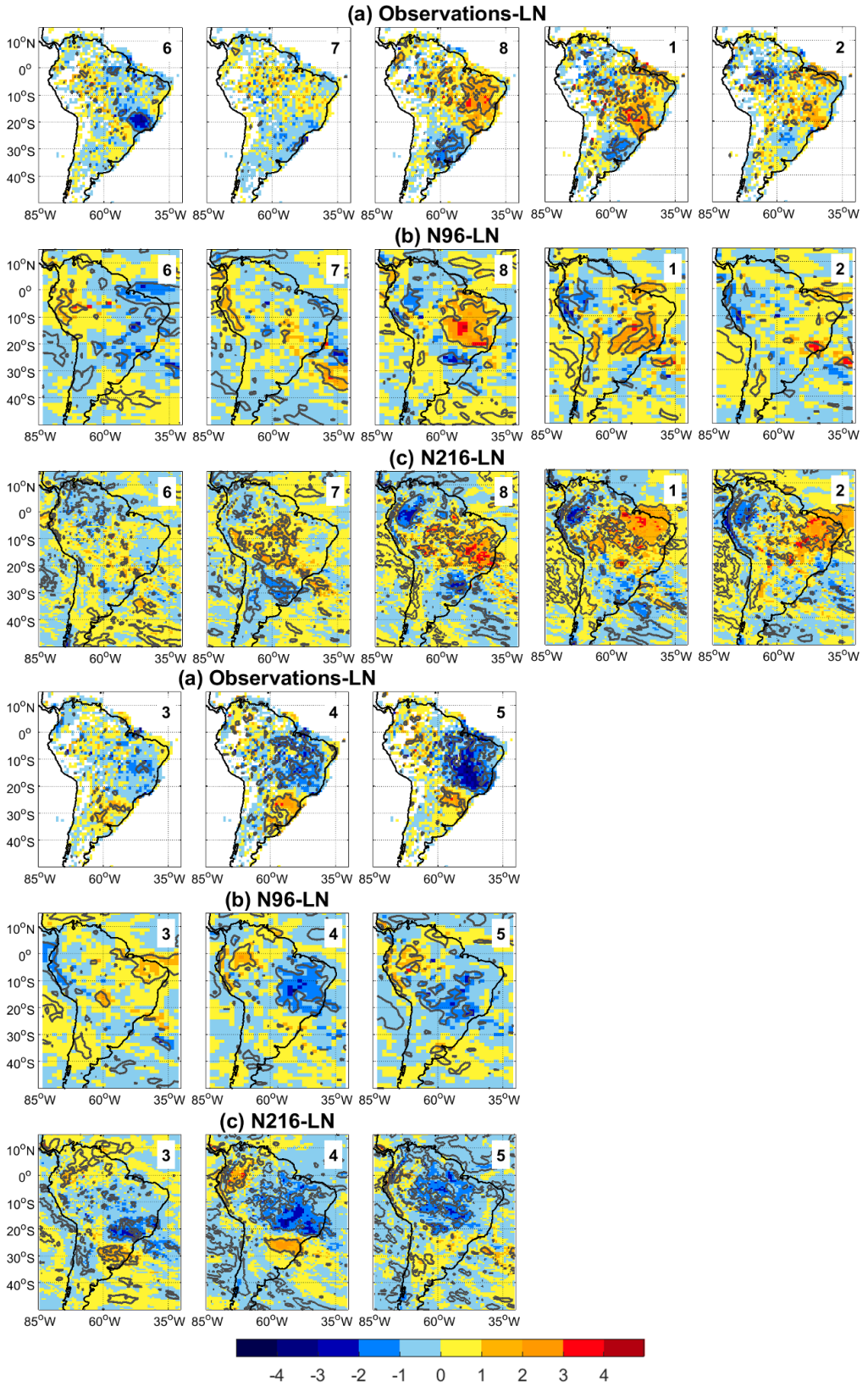

Figure 13. Same as Figure 7, but for (a) observations-LN, (b) N96-LN, and (c) N216-LN.

6 Conclusions

This study has evaluated the MJO, its impacts on SA, and their modulation by ENSO in MetUM-GOML3 during austral summer (DJF). MetUM-GOML3 simulates well the distribution of MJO activity in RMM phase space (Fig. 2b-c), and reproduces changes in MJO activity when the ENSO-related anomalies favor/oppose certain MJO phases (Fig. 2e-f,h-i). We found errors in the convection-circulation phase relationship since the model achieves the same RMM phase but simulates convection further east than observed (Fig. 3), with the dynamical wave feedback likely quicken MJO propagation. The fully established tropical (Fig. 5) and extratropical (Fig. 6) teleconnections to SA, the strongest convection (Fig. 3), and positive precipitation anomalies over CESA (Fig. 7) during phase 1 (Grimm, 2019) happen earlier in MetUM-GOML3 (phase 8), and several aspects of the model support the shifting of the MJO teleconnections to one phase earlier. In phase 4, MetUM-GOML3 also simulates suppressed convection and low-level divergence over the CSSP (Fig. 3b-c) triggering the extratropical teleconnection to SA opposite-signed with respect to phase 8 (Fig. 6b-c) and its impacts on SA (Fig. 7b-c).

The model reproduces the ENSO influence on both the basic state and the MJO convective anomalies, which modulate the MJO teleconnections and their impacts on SA. The MJO structure (Fig. 8,9) and circulation anomalies (Figs. 10,11) are more (less) robust in EN (LN) with respect to simulations without ENSO (Figs. 3,4,5,6), improving (worsening) the depiction of the equatorial waves and the eastward MJO propagation (Fig. 9), coherent with the smaller (larger) MJO decay over the Maritime Continent (Fig. 2e-f,h-i). Stronger enhanced (suppressed) MJO convection appears over the CSSP in simulations with ENSO in phase 8 (phase 4) (Fig. 8), exciting stronger extratropical teleconnections (Fig. 11) with respect to those in simulations without ENSO (Figs. 3,6). Moreover, the model reproduces the convection over

769 the CSSP peaking earlier and more to the west in LN (phases 7-8) than EN (phases 8-1),
770 coherent with observations. When MetUM-GOML3 improves the simulation of the MJO
771 convection and teleconnections under the active ENSO states (Figs. 8,9,10,11), the magnitude
772 and spatial distribution of the precipitation anomalies over SA improves (Figs. 12,13). Also,
773 when the model reproduces similar anomalous MJO patterns pointed out in observations
774 (Fernandes & Grimm, 2023) it validates the physical mechanisms proposed for ENSO
775 modulation of the MJO impacts, particularly because simulations provide a larger sample of
776 ENSO events than that from observed records.

777 Hence, MetUM-GOML3 has shown valuable skill in simulating the MJO teleconnections
778 in phases 8 and 4 and their opposite impacts on SA, and this ability is even higher when ENSO is
779 active. As the MJO and its teleconnections improve during EN, other CGCMs may reproduce
780 these features, and S2S predictions to SA may be better when EN and MJO peak in DJF, though
781 the MJO impacts in phase 1 remain challenging.

782 **Acknowledgments**

783 L. G. F. was supported by Coordination for the Improvement of Higher Education Personnel
784 (CAPES-Brazil) and by the Newton Fund through the Met Office Climate Science for Service
785 Partnership Brazil (CSSP Brazil). A. M. G. received financial support from the National Council
786 for Scientific and Technological Development (CNPq-Brazil). N. P. K. was funded by an
787 Independent Research Fellowship from the Natural Environment Research Council
788 (NE/L010976/1) and by the NERC/GCRF programme Atmospheric hazard in developing
789 countries: risk assessment and early warnings (ACREW).

790 **Data Availability Statement**

The observed precipitation can be obtained from the website (https://www.snirh.gov.br/hidroweb/serieshistoricas). NOAA interpolated OLR data can be obtained from the https://psl.noaa.gov/data/gridded/data.olrcdr.interp.html website. ERA-Interim reanalysis can be obtained from the https://www.ecmwf.int/en/forecasts/datasets/reanalysis-datasets/era-interim website. The Smith and Murphy (2007) ocean analyses and data from all simulations analyzed are stored on the JASMIN collaborative analysis facility (http://jasmin.ac.uk).

References

Ahn, M.S. et al. (2017), MJO simulation in CMIP5 climate models: MJO skill metrics and process-oriented diagnosis. *Climate Dynamics,* 49(11–12), 4023–4045. doi:10.1007/s00382-017-3558-4

Ahn, M.S. et al. (2020), MJO propagation across the Maritime Continent: Are CMIP6 models better than CMIP5 models? *Geophysical Research Letters,* 47, e2020GL087250. doi:10.1029/2020GL087250

Arcodia, M.C. et al. (2020), How MJO Teleconnections and ENSO Interference Impacts U.S. Precipitation. *Journal of Climate,* 33, 4621–4640. doi:10.1175/JCLI-D-19-0448.1

Alvarez, M.S. et al. (2015), Influence of the Madden Julian Oscillation on precipitation and surface air temperature in South America. *Climate Dynamics,* 46(1–2), 245–262. doi:10.1007/s00382-015-2581-6

Barreiro, M., Chang, P., & Saravan R. (2002), Variability of the South Atlantic Convergence Zone Simulated by an Atmospheric General Circulation Model. *Journal of Climate,* 15, 745–763. doi: 10.1175/1520-0442(2002)015<0745:VOTSAC>2.0.CO;2

812 Barreiro, M. et al. (2018), Modelling the role of Atlantic air-sea interaction in the impact of the
813 Madden-Julian Oscillation on South American climate. *International Journal Climatology*, 1–13.
814 doi:10.1002/joc.5865

815 Bush, S.J. et al. (2015), The effect of increased convection entrainment on Asian monsoon biases
816 in the MetUM general circulation model. *Quarterly Journal of the Royal Meteorological Society,*
817 141, 311–326. doi:10.1002/qj.237

818 Carvalho, L.M.V., Jones, C., & Liebmann, B. (2004), The South Atlantic convergence zone:
819 Intensity, form, persistence, and relationships with intraseasonal to interannual activity and
820 extreme rainfall. *Journal of Climate,* 17(1), 88–108. doi:10.1175/1520-
821 0442(2004)017<0088:TSACZI>2.0.CO;2

822 Chen, G., & Wang, B. (2018), Effects of Enhanced Front Walker Cell on the Eastward
823 Propagation of the MJO. *Journal of Climate,* 31, 7719–7738. doi:10.1175/JCLI-D-17-0383.1

824 Coelho, C.A.S. et al. (2020), Evaluation of climate simulations produced with the Brazilian
825 global atmospheric model version 1.2. *Climate Dynamics.* doi:10.1007/s00382-020-05508-8

826 Craig, A., Valcke, S., & Coquart L. (2017), Development and performance of a new version of
827 the OASIS coupler, OASIS3-MCT_3.0. *Geoscientific Model Development,* 3297–3308.
828 doi:10.5194/gmd-10-3297-2017

829 Cunningham, C.A.C., & Cavalcanti, I.F.A. (2006), Intraseasonal modes of variability affecting
830 the South Atlantic Convergence Zone. *International Journal of Climatology,* 26(9), 1165–1180.
831 doi:10.1002/joc.1309

832 Dawson, A. (2016), Windspharm: A High-Level Library for Global Wind Field Computations
833 Using Spherical Harmonics. *Journal of Open Research Software,* 4. doi:10.5334/jors.129

834 Dee, D.P. et al. (2011), The ERA-Interim reanalysis: Configuration and performance of the data
835 assimilation system. *Quarterly Journal of the Royal Meteorological Society,* 137(656), 553–597.
836 doi:10.1002/qj.828

837 Delworth, T.L. et al. (2012), Simulated climate and climate change in the GFDL CM2.5 high-
838 resolution coupled climate model. *Journal of Climate,* 25(8), 2755–2781. doi:10.1175/JCLI-D-
839 11-00316.1

840 DeMott, C.A., Klingaman, N.P., & Woolnough, S. J. (2015), Atmosphere-ocean coupled
841 processes in the Madden-Julian oscillation. *Reviews of Geophysics.* doi:10.1002/2014RG000478

842 Diaz, N., Barreiro, M., & Rubido, N. (2022) The Distinct Influence of Two Madden-Julian
843 Trajectory Classes on the South American Dipole. *Journal of Climate*, 35, 7093–7107. doi:
844 10.1175/JCLI-D-21-1001.1

845 Duchon, C.E. (1979), Lanczos Filtering in One and Two Dimensions. *Journal of Applied*
846 *Meteorology,* 1016–1022. doi:10.1175/1520-0450(1979)018<1016:LFIOAT>2.0.CO;2

847 Fernandes, L.G., & Grimm A.M. (2023), Global ENSO modulation of MJO and its impacts on
848 South America. *Journal of Climate.* doi:10.1175/JCLI-D-22-0781.1

849 Ghelani, R.P.S. et al. (2017), Joint Modulation of Intraseasonal Rainfall in Tropical Australia by
850 the Madden-Julian Oscillation and El Niño-Southern Oscillation. *Geophysical Research Letters,*
851 44(20), 10,754–10,761. doi:10.1002/2017GL075452

852 Giddings, J. et al. (2020), The effect of seasonally and spatially varying chlorophyll on Bay of
853 Bengal surface ocean properties and the South Asian monsoon. *Weather and Climate Dynamics,*
854 1, 635–655. doi:10.5194/wcd-1-635-2020

855 Grimm, A.M. (2003), The El Niño impact on the summer monsoon in Brazil: Regional processes
856 versus remote influences. *Journal of Climate,* 16(2), 263–280. doi:10.1175/1520-
857 0442(2003)016<0263:TENIOT>2.0.CO;2

858 Grimm, A.M. (2004), How do La Niña events disturb the summer monsoon system in Brazil,
859 *Climate Dynamics,* 22(2–3), 123–138. doi:10.1007/s00382-003-0368-7

860 Grimm, A.M. (2019), Madden–Julian Oscillation impacts on South American summer monsoon
861 season: precipitation anomalies, extreme events, teleconnections, and role in the MJO cycle.
862 *Climate Dynamics,* 53(1–2), 907–932. doi:10.1007/s00382-019-04622-6

863 Grimm, A.M., Hakoyama, L.R., & Scheibe, L.A. (2021), Active and break phases of the South
864 American summer monsoon: MJO influence and subseasonal prediction. *Climate Dynamics,*
865 (0123456789). doi:10.1007/s00382-021-05658-3

866 Grimm, A.M., Pal, J.S. and Giorgi, F. (2007), Connection between spring conditions and peak
867 summer monsoon rainfall in South America: Role of soil moisture, surface temperature, and
868 topography in eastern Brazil. *Journal of Climate,* 20(24), 5929–5945.
869 doi:10.1175/2007JCLI1684.1

870 Grimm, A.M., & Silva Dias, P.L. (1995), Analysis of tropical-extratropical interactions with
871 influence functions of a barotropic model. *Journal of Atmospheric Sciences,* 3538–3555.
872 doi:10.1175/1520-0469(1995)052<3538:AOTIWI>2.0.CO;2

873 Henderson, S.A., Maloney, E.D., & Son, S.W. (2017), Madden-Julian oscillation Pacific
874 teleconnections: The impact of the basic state and MJO representation in general circulation
875 models. *Journal of Climate,* 30(12), 4567–4587. doi:10.1175/JCLI-D-16-0789.1

876 Henderson, S.A., & Maloney, E.D., & Son, S.W. (2018), The Impact of the Madden-Julian
877 Oscillation on High-Latitude Winter Blocking during El Niño-Southern Oscillation Events.
878 *Journal of Climate,* 31, 5293–5318. doi:10.1175/JCLI-D-17-0721.1

879 Hendon, H.H., Zhang, C., & Glick, J.D. (1999), Interannual variation of the Madden-Julian
880 oscillation during austral summer. *Journal of Climate,* 12(8 PART 2), 2538–2550.
881 doi:10.1175/1520-0442(1999)012<2538:ivotmj>2.0.co;2

882 Hertwig, E. et al. (2015), Effect of horizontal resolution on ECHAM6-AMIP performance.
883 *Climate Dynamics*, 45, 185–211. doi:10.1007/s00382-014-2396-x

884 Hirata, F.E., & Grimm, A.M. (2015), The role of synoptic and intraseasonal anomalies in the life
885 cycle of summer rainfall extremes over South America. *Climate Dynamics,* 46(9–10), 3041–
886 3055. doi:10.1007/s00382-015-2751-6

887 Hirons, L.C., Klingaman, N.P., & Woolnough, S.J. (2015), MetUM-GOML1: A near-globally
888 coupled atmosphere-ocean-mixed-layer model. *Geoscientific Model Development,* 8(2), 363–
889 379. doi:10.5194/gmd-8-363-2015

890 Jiang, X. et al. (2015), Vertical structure and physical processes of the Madden-Julian
891 oscillation: Exploring key model physics in climate simulations. *Journal of Geophysical*
892 *Research,* 120, 4718–4748. doi:10.1002/2014JD022375

893 Jung, T. et al. (2012), High-resolution global climate simulations with the ECMWF model in
894 project athena: Experimental design, model climate, and seasonal forecast skill. *Journal of*
895 *Climate,* 25(9), 3155–3172. doi:10.1175/JCLI-D-11-00265.1

896 Kessler, W.S. (2001), EOF Representations of the Madden-Julian Oscillation and Its Connection
897 with ENSO. *Journal of Climate,* 14, 3055-3061. doi:10.1175/1520-
898 0442(2001)014<3055:EROTMJ>2.0.CO;2

899 Kim, D., Kug, J.-S., & Sobel, A.H. (2011), A systematic relationship between intraseasonal
900 variability and mean state bias in AGCM simulations. *Journal of Climate,* 24(21), 5506–5520.
901 doi:10.1175/2011JCLI4177.1

902 Kim, D. et al. (2014), Propagating versus nonpropagating Madden–Julian oscillation events.
903 *Journal of Climate,* 27, 111–125. doi:10.1175/JCLI-D-13-00084.1

904 Kim, D., Kim, H., & Lee, M.I. (2017), Why does the MJO detour the Maritime Continent during
905 austral summer? *Geophysical Research Letters,* 44(5), 2579–2587. doi:10.1002/2017GL072643

906 Kim, H., Vitart, F., & Waliser, D.E. (2018), Prediction of the Madden-Julian oscillation: A
907 review. *Journal of Climate,* 31(23), 9425–9443. doi:10.1175/JCLI-D-18-0210.1

908 Klingaman, N.P. et al. (2015), Vertical structure and physical processes of the Madden-Julian
909 oscillation: Linking hindcast fidelity to simulated diabatic heating and moistening. *Journal of*
910 *Geophysical Research,* 120(10), 4690–4717. doi:10.1002/2014JD022374

911 Klingaman, N.P. et al. (2020), Subseasonal Prediction Performance for Austral Summer South
912 American Rainfall. *Weather and Forecasting,* 36(1), 147–169. doi:10.1175/waf-d-19-0203.1

913 Klingaman, N.P., & Demott, C.A. (2020), Mean State Biases and Interannual Variability Affect
914 Perceived Sensitivities of the Madden-Julian Oscillation to Air-Sea Coupling. *Journal of*
915 *Advances in Modeling Earth Systems,* 12(2), 1–22. doi:10.1029/2019MS001799

916 Klingaman, N.P., & Woolnough, S.J. (2014a), The role of air – sea coupling in the simulation of
917 the Madden – Julian oscillation in the Hadley Centre model. 2272–2286. doi:10.1002/qj.2295

918 Klingaman, N.P., & Woolnough, S.J. (2014b), Using a case-study approach to improve the
919 Madden-Julian oscillation in the Hadley Centre model. *Quarterly Journal of the Royal*
920 *Meteorological Society,* 140(685), 2491–2505. doi:10.1002/qj.2314

921 Kodama, C. et al. (2015), A 20-Year climatology of a NICAM AMIP-type simulation. *Journal of*
922 *the Meteorological Society of Japan,* 93(4), 393–424. doi:10.2151/jmsj.2015-024

923 Large, W.G., McWilliams, J.C., & Doney, S.C. (1994), Oceanic vertical mixing: A review and a
924 model with a nonlocal boundary layer parameterization. *Reviews of Geophysics,* 32(4), 363–403.
925 doi:10.1029/94RG01872

926 Lee, R.W. et al. (2019), ENSO Modulation of MJO Teleconnections to the North Atlantic and
927 Europe. *Geophysical Research Letters,* 46(22), 13535–13545. doi:10.1029/2019GL084683

928 Liebmann, B., & Allured, D. (2005), Daily precipitation grids for South America. *Bulletin of the*
929 *American Meteorological Society,* 86(11), 1567–1570. doi:10.1175/BAMS-86-11-1567

930 Liebmann B., & Smith C.A. (1996), Description of a Complete (Interpolated) Outgoing
931 Longwave Radiation Dataset. *Bulletin of the American Meteorological Society,* 77, 1275–1277.

932 Liu, F., & Wang B. (2017), Roles of the Moisture and Wave Feedbacks in Shaping the Madden-
933 Julian Oscillation. *Journal of Climate,* 30, 10275–10291.

934 Liu, X. et al. (2017), MJO prediction using the sub-seasonal to seasonal forecast model of
935 Beijing Climate Center. *Climate Dynamics,* 48(9–10), 3283–3307. doi:10.1007/s00382-016-
936 3264-7

937 Martin-Gomez V., & Barreiro M. (2020), The influence of nonlinearities and different SST
938 spatial patterns on the summertime anomalies in subtropical South America during strong ENSO
939 events. *Climate Dynamics*, 54, 3765–3779. doi:10.1007/s00382-020-05201-w

940 Matsuno, T. (1966), Quasi-Geostrophic Motions in the Equatorial Area. *Journal of the*
941 *Meteorological Society of Japan.* Ser. II, 44(1), 25–43. doi:10.2151/jmsj1965.44.1_25

942 Monerie, P.-A. et al. (2020), Role of atmospheric horizontal resolution in simulating tropical and
943 subtropical South American precipitation in HadGEM3-GC31. *Geoscientific Model*
944 *Development Discussions*, (June), 1–44. doi:10.5194/gmd-2020-125

945 Moon, J.Y., Wang, B., & Ha, K.J. (2011), ENSO regulation of MJO teleconnection. *Climate*
946 *Dynamics,* 37(5), 1133–1149. doi:10.1007/s00382-010-0902-3

947 Müller, W.A. et al. (2018), A Higher-resolution Version of the Max Planck Institute Earth
948 System Model (MPI-ESM 1.2-HR). *Journal of Advances in Modeling Earth Systems*, 10, 1383–
949 1413. doi:10.1029/2017MS001217

950 Peatman, S.C., & Klingaman, N.P. (2018), The Indian summer monsoon in MetUM-GOML2.0:
951 effects of air-sea coupling and resolution. *Geoscientific Model Development,* 11, 4693–4709.
952 doi:10.5194/gmd-11-4693-2018

953 Rayner, N.A. et al. (2003), Global analyses of sea surface temperature, sea ice, and night marine
954 air temperature since the late nineteenth century. *Journal of Geophysical Research D:*
955 *Atmospheres,* 108(14). doi:10.1029/2002jd002670

956 Roundy, P.E. et al. (2010), Modulation of the global atmospheric circulation by combined
957 activity in the Madden-Julian oscillation and the El Niño-southern oscillation during boreal
958 winter. *Journal of Climate,* 23(15), 4045–4059. doi:10.1175/2010JCLI3446.1

959 Sakaeda, N., & Roundy, P.E. (2016), The development of upper-tropospheric geopotential height
960 anomaly in the Western Hemisphere during MJO convective initiations. *Quarterly Journal of the*
961 *Royal Meteorological Society,* 142(695), 942–956. doi:10.1002/qj.2696

962 Slingo, J.M. et al. (1999), On the predictability of the interannual behaviour of the Madden-
963 Julian Oscillation and its relationship with El Nino. *Quarterly Journal of the Royal*
964 *Meteorological Society,* 125(554), 583–609. doi:10.1256/smsqj.55410

965 Smith, D.M., & Murphy, J.M. (2007), An objective ocean temperature and salinity analysis using
966 covariances from a global climate model. *Journal of Geophysical Research,* 12(C02022).
967 doi:10.1029/2005JC003172

968 Solman, S.A., & Blázquez, J. (2019), Multiscale precipitation variability over South America:
969 Analysis of the added value of CORDEX RCM simulations. *Climate Dynamics,* 53(3–4), 1547–
970 1565. doi:10.1007/s00382-019-04689-1

971 Souza Custodio, M.S., Rocha, R.P., & Vidale, P.L. (2012), Analysis of precipitation climatology
972 simulated by high resolution coupled global models over the South America. *Hydrological*
973 *Research Letters,* 6(0), 92–97. doi:10.3178/hrl.6.92

974 Souza Custodio, M. et al. (2017), Impact of increased horizontal resolution in coupled and
975 atmosphere-only models of the HadGEM1 family upon the climate patterns of South America.
976 *Climate Dynamics,* 48(9–10), 3341–3364. doi:10.1007/s00382-016-3271-8

977 Straub, K.H. (2013), MJO Initiation in the Real-Time Multivariate MJO Index. *Journal of*
978 *Climate,* 26, 1130–1151. doi:10.1175/JCLI-D-12-00074.1

979 Suematsu, T., & Miura H. (2022), Changes in the Eastward Movement Speed of the Madden-
980 Julian Oscillation with Fluctuation in the Walker Circulation. *Journal of Climate*, 35, 211–225.
981 doi: 10.1175/JCLI-D-21-0269.1

982 Tam, C.Y., & Lau, N.C. (2005), Modulation of the Madden-Julian Oscillation by ENSO:
983 Inferences from observations and GCM simulations. *Journal of the Meteorological Society of*
984 *Japan,* 83(5), 727–743. doi:10.2151/jmsj.83.727

985 Tseng, K.C., Maloney, E., & Barnes, E.A. (2020), The consistency of MJO teleconnection
986 patterns on interannual time scales. *Journal of Climate,* 33(9), 3471–3486. doi:10.1175/JCLI-D-
987 19-0510.1

988 Vitart, F. et al. (2017), The subseasonal to seasonal (S2S) prediction project database. *Bulletin of*
989 *the American Meteorological Society,* 98(1), 163–173. doi:10.1175/BAMS-D-16-0017.1

990 Vitart, F. and Molteni, F. (2010), Simulation of the Madden-Julian oscillation and its
991 teleconnections in the ECMWF forecast system. *Quarterly Journal of the Royal Meteorological*
992 *Society,* 136(649), 842–855. doi:10.1002/qj.623

993 Vitart, F., Robertson, A.W., & S2S Steering Group (2015), Sub-seasonal to seasonal prediction:
994 Linking weather and climate. *In Seamless Prediction of the Earth System: From Minutes to*

995 *Months* (pp. 385–401). WMO-1156, World Meteorological Organization.
996 http://library.wmo.int/pmb_ged/wmo_1156_en.pdf.

997 Walters, D. et al. (2019), The Met Office Unified Model Global Atmosphere 7.0/7.1 and JULES
998 Global Land 7.0 configurations. *Geoscientific Model Development,* 12(5), 1909–1963.
999 doi:10.5194/gmd-12-1909-2019

1000 Wang, J. et al. (2020a), MJO teleconnections over the PNA region in climate models. Part I:
1001 Performance- And process-based skill metrics. *Journal of Climate,* 33(3), 1051–1067.
1002 doi:10.1175/JCLI-D-19-0253.1

1003 Wang, J. et al. (2020b), MJO Teleconnections over the PNA Region in Climate Models. Part II:
1004 Impacts of the MJO and Basic State. *Journal of Climate,* 33(12), 5081–5101. doi:10.1175/jcli-d-
1005 19-0865.1

1006 Wang, L., Li, T., & Nasuno, T. (2018), Impact of Rossby and Kelvin Wave Components on MJO
1007 Eastward Propagation. *Journal of Climate,* 31, 6913–6931. doi:10.1175/JCLI-D-17-0749.1

1008 Wei Y, Ren H-L (2019), Modulation of ENSO on Fast and Slow MJO Modes during Boreal
1009 Winter. *Journal of Climate,* 32, 7483–7506. doi:10.1175/JCLI-D-19-0013.1

1010 Wheeler, M.C., & Hendon, H.H. (2004), An all-season real-time multivariate MJO index:
1011 Development of an index for monitoring and prediction. *Monthly Weather Review,* 132(8),
1012 1917–1932. doi:10.1175/1520-0493(2004)132<1917:AARMMI>2.0.CO;2

1013 Wheeler, M.C. et al. (2009), Impacts of the Madden-Julian Oscillation on Australian Rainfall and
1014 Circulation, *Journal of Climate,* 22, 1482–1498. doi:10.1175/2008JCLI2595.1

1015 Wilks, D.S. (2006). *Statistical Methods in the Atmospheric Sciences*. United States of America:
1016 Academic Press.

1017 Zhang, C. (2005), MADDEN-JULIAN OSCILLATION. *Reviews of Geophysics.* 1–36.
1018 doi:10.1029/2004RG000158.1.INTRODUCTION

1019 Zhang, C. and Ling, J. (2017), Barrier effect of the Indo-Pacific Maritime Continent on the MJO:
1020 Perspectives from tracking MJO precipitation. *Journal of Climate,* 30(9), 3439–3459.
1021 doi:10.1175/JCLI-D-16-0614.1

1022 Zhang, C. et al. (2020), Four Theories of the Madden-Julian Oscillation. *Review of Geophysics,*
1023 58, e2019RG000685. doi:10.1029/2019RG000685

Figure 1.

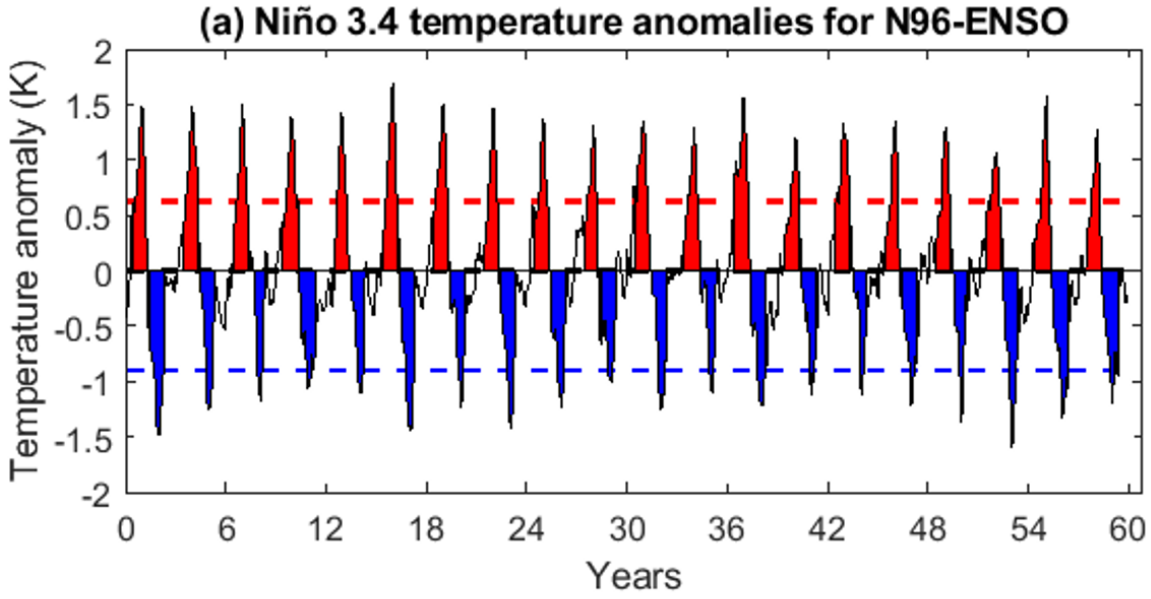
(a) Niño 3.4 temperature anomalies for N96-ENSO
Temperature anomaly (K)
2
1.5
1
0.5
0
-0.5
-1
-1.5
-2
0
6
12
18
24
30
36
42
48
54
60
Years

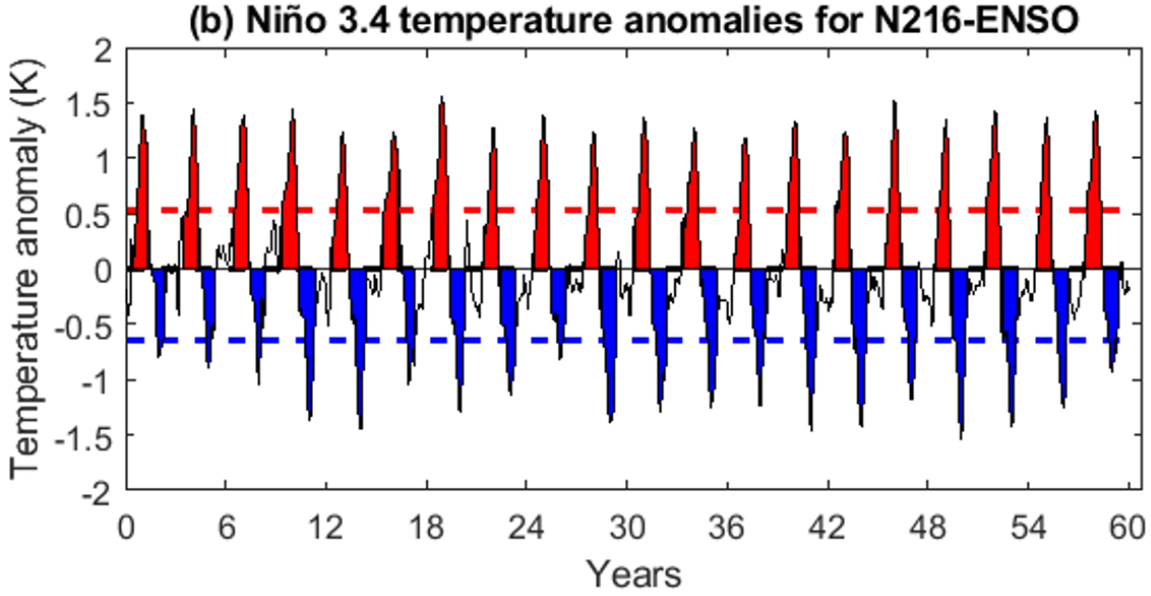
(b) Niño 3.4 temperature anomalies for N216-ENSO
Temperature anomaly (K)
2
1.5
1
0.5
0
-0.5
-1
-1.5
-2
0
6
12
18
24
30
36
42
48
54
60
Years

Figure 2.

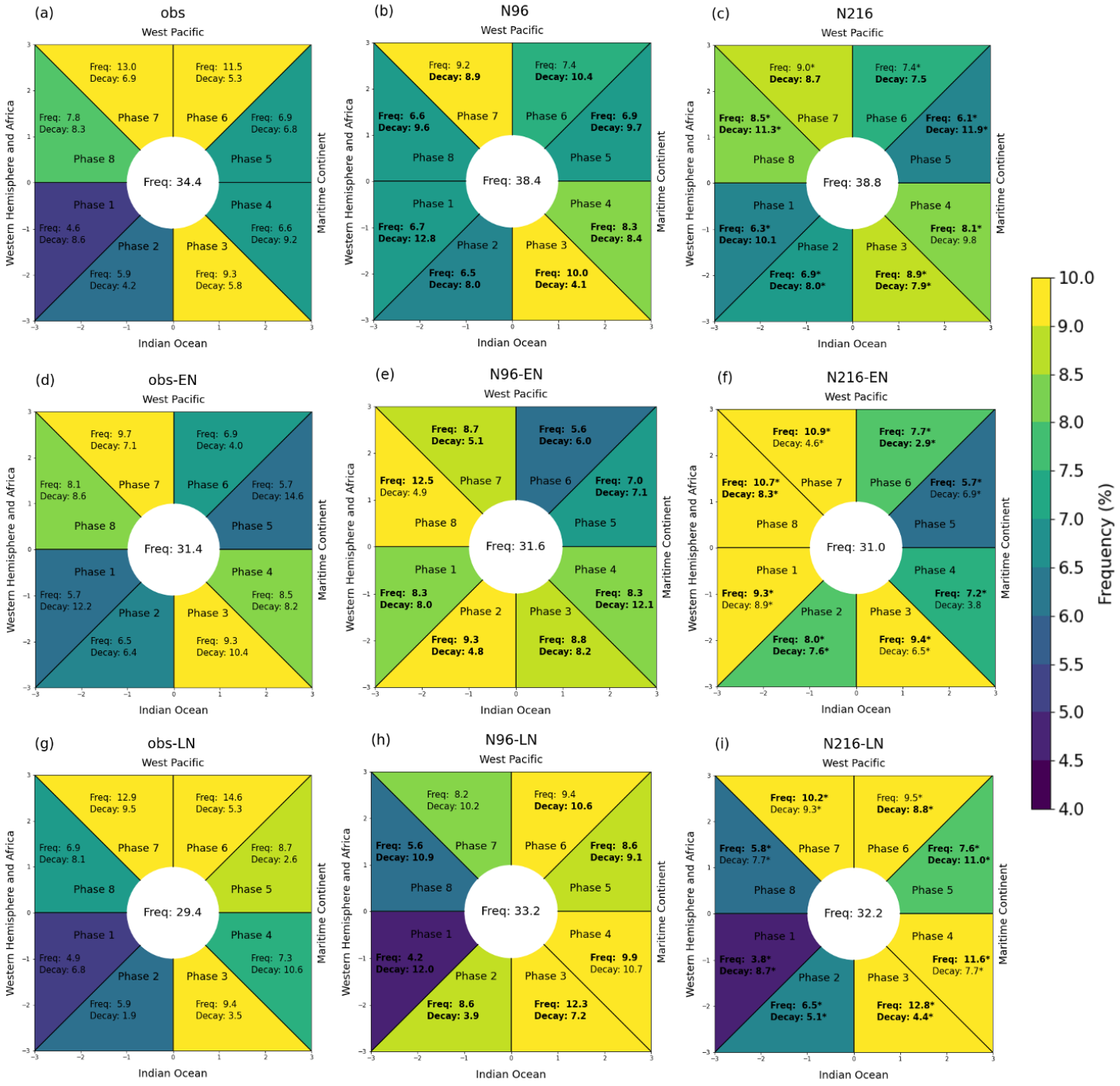
(a) obs
West Pacific
Freq: 13.0
Decay: 6.9
Freq: 11.5
Decay: 5.3
Freq: 7.8
Decay: 8.3
Phase 7
Phase 6
Freq: 6.9
Decay: 6.8
Phase 8
Phase 5
Freq: 34.4
Phase 1
Phase 4
Freq: 4.6
Decay: 8.6
Phase 2
Phase 3
Freq: 6.6
Decay: 9.2
Freq: 5.9
Decay: 4.2
Freq: 9.3
Decay: 5.8
Western Hemisphere and Africa
Maritime Continent
Indian Ocean
(b) N96
West Pacific
Freq: 9.2
Decay: 8.9
Freq: 7.4
Decay: 10.4
Freq: 6.6
Decay: 9.6
Phase 7
Phase 6
Freq: 6.9
Decay: 9.7
Phase 8
Phase 5
Freq: 38.4
Phase 1
Phase 4
Freq: 6.7
Decay: 12.8
Phase 2
Phase 3
Freq: 8.3
Decay: 8.4
Freq: 6.5
Decay: 8.0
Freq: 10.0
Decay: 4.1
Western Hemisphere and Africa
Maritime Continent
Indian Ocean
(c) N216
West Pacific
Freq: 9.0*
Decay: 8.7
Freq: 7.4*
Decay: 7.5
Freq: 8.5*
Decay: 11.3*
Phase 7
Phase 6
Freq: 6.1*
Decay: 11.9*
Phase 8
Phase 5
Freq: 38.8
Phase 1
Phase 4
Freq: 6.3*
Decay: 10.1
Phase 2
Phase 3
Freq: 8.1*
Decay: 9.8
Freq: 6.9*
Decay: 8.0*
Freq: 8.9*
Decay: 7.9*
Western Hemisphere and Africa
Maritime Continent
Indian Ocean
(d) obs-EN
West Pacific
Freq: 9.7
Decay: 7.1
Freq: 6.9
Decay: 4.0
Freq: 8.1
Decay: 8.6
Phase 7
Phase 6
Freq: 5.7
Decay: 14.6
Phase 8
Phase 5
Freq: 31.4
Phase 1
Phase 4
Freq: 5.7
Decay: 12.2
Phase 2
Phase 3
Freq: 8.5
Decay: 8.2
Freq: 6.5
Decay: 6.4
Freq: 9.3
Decay: 10.4
Western Hemisphere and Africa
Maritime Continent
Indian Ocean
(e) N96-EN
West Pacific
Freq: 8.7
Decay: 5.1
Freq: 5.6
Decay: 6.0
Freq: 12.5
Decay: 4.9
Phase 7
Phase 6
Freq: 7.0
Decay: 7.1
Phase 8
Phase 5
Freq: 31.6
Phase 1
Phase 4
Freq: 8.3
Decay: 8.0
Phase 2
Phase 3
Freq: 8.3
Decay: 12.1
Freq: 9.3
Decay: 4.8
Freq: 8.8
Decay: 8.2
Western Hemisphere and Africa
Maritime Continent
Indian Ocean
(f) N216-EN
West Pacific
Freq: 10.9*
Decay: 4.6*
Freq: 7.7*
Decay: 2.9*
Freq: 10.7*
Decay: 8.3*
Phase 7
Phase 6
Freq: 5.7*
Decay: 6.9*
Phase 8
Phase 5
Freq: 31.0
Phase 1
Phase 4
Freq: 9.3*
Decay: 8.9*
Phase 2
Phase 3
Freq: 7.2*
Decay: 3.8
Freq: 8.0*
Decay: 7.6*
Freq: 9.4*
Decay: 6.5*
Western Hemisphere and Africa
Maritime Continent
Indian Ocean
(g) obs-LN
West Pacific
Freq: 12.9
Decay: 9.5
Freq: 14.6
Decay: 5.3
Freq: 6.9
Decay: 8.1
Phase 7
Phase 6
Freq: 8.7
Decay: 2.6
Phase 8
Phase 5
Freq: 29.4
Phase 1
Phase 4
Freq: 4.9
Decay: 6.8
Phase 2
Phase 3
Freq: 7.3
Decay: 10.6
Freq: 5.9
Decay: 1.9
Freq: 9.4
Decay: 3.5
Western Hemisphere and Africa
Maritime Continent
Indian Ocean
(h) N96-LN
West Pacific
Freq: 8.2
Decay: 10.2
Freq: 9.4
Decay: 10.6
Freq: 5.6
Decay: 10.9
Phase 7
Phase 6
Freq: 8.6
Decay: 9.1
Phase 8
Phase 5
Freq: 33.2
Phase 1
Phase 4
Freq: 4.2
Decay: 12.0
Freq: 9.9
Decay: 10.7
Phase 2
Phase 3
Freq: 8.6
Decay: 3.9
Freq: 12.3
Decay: 7.2
Western Hemisphere and Africa
Maritime Continent
Indian Ocean
(i) N216-LN
West Pacific
Freq: 10.2*
Decay: 9.3*
Freq: 9.5*
Decay: 8.8*
Freq: 5.8*
Decay: 7.7*
Phase 7
Phase 6
Freq: 7.6*
Decay: 11.0*
Phase 8
Phase 5
Freq: 32.2
Phase 1
Phase 4
Freq: 3.8*
Decay: 8.7*
Phase 2
Phase 3
Freq: 11.6*
Decay: 7.7*
Freq: 6.5*
Decay: 5.1*
Freq: 12.8*
Decay: 4.4*
Western Hemisphere and Africa
Maritime Continent
Indian Ocean
Frequency (%)
10.0
9.0
8.5
8.0
7.5
7.0
6.5
6.0
5.5
5.0
4.5
4.0

Figure 3.

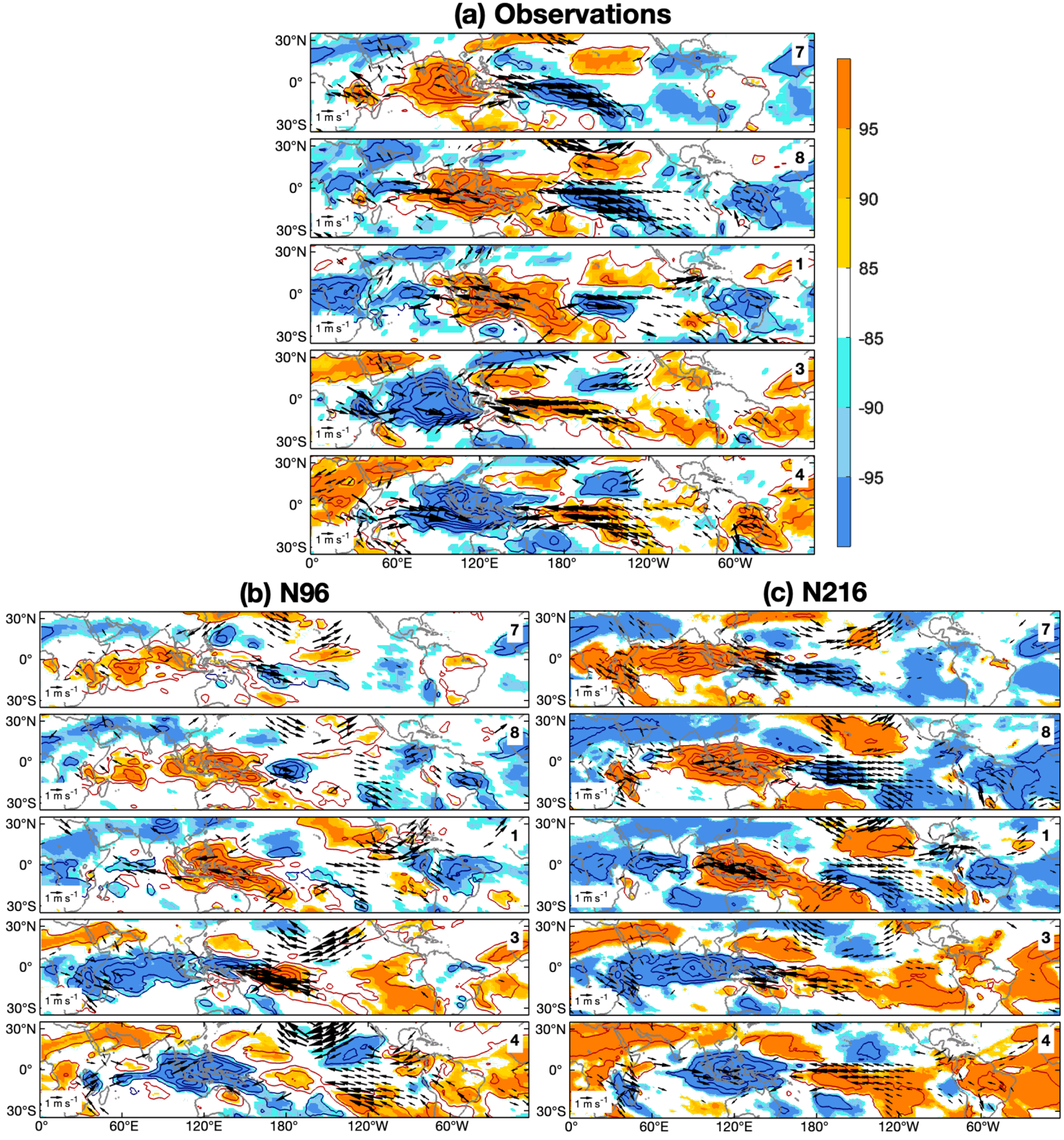
(a) Observations
(b) N96
(c) N216
7
8
1
3
4
95
90
85
-85
-90
-95
30°N
0°
30°S
0°
60°E
120°E
180°
120°W
60°W
1 m s-1

Figure 4.

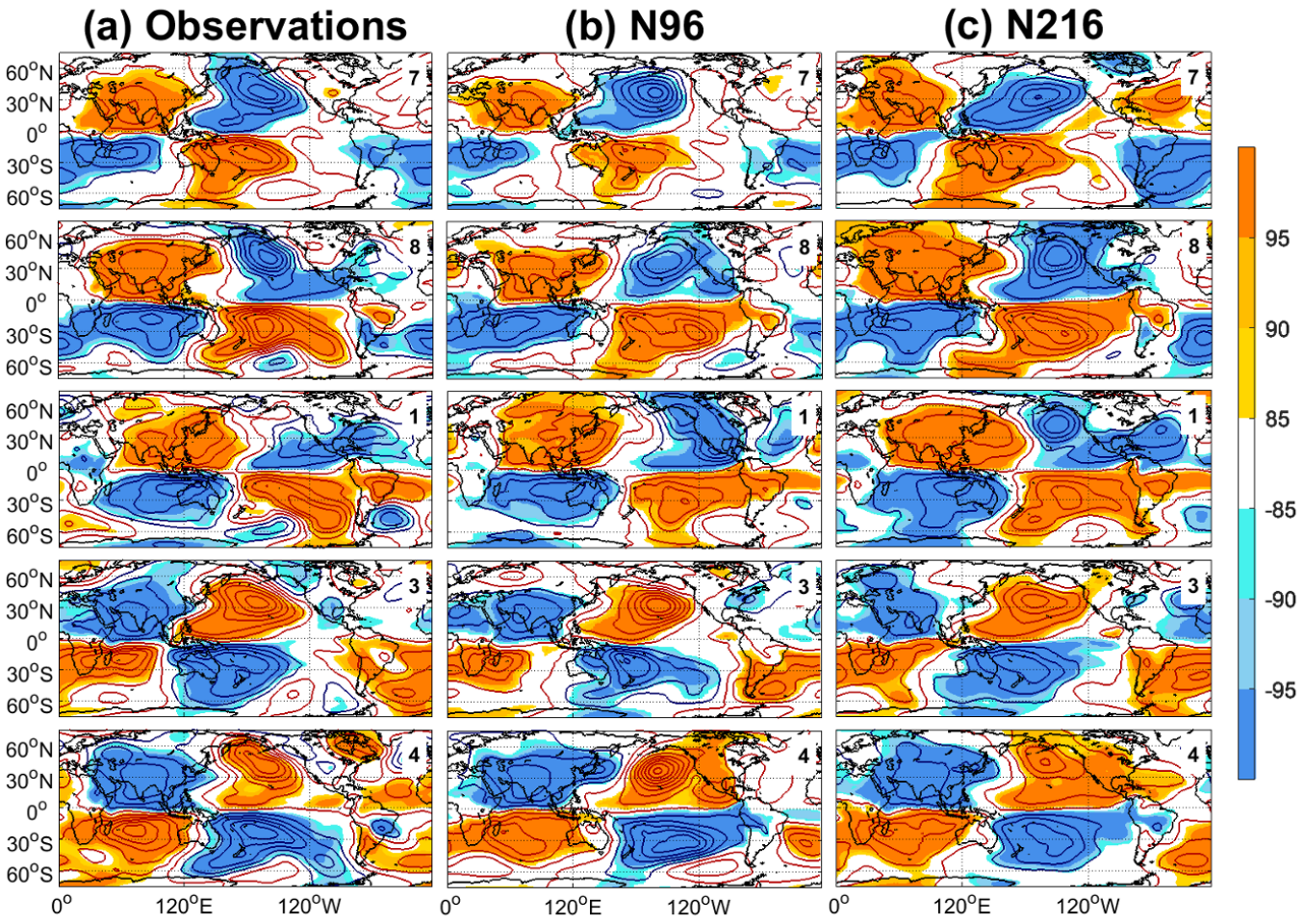
(a) Observations
(b) N96
(c) N216
60°N
30°N
0°
30°S
60°S
7
8
1
3
4
0°
120°E
120°W
95
90
85
-85
-90
-95

Figure 5.

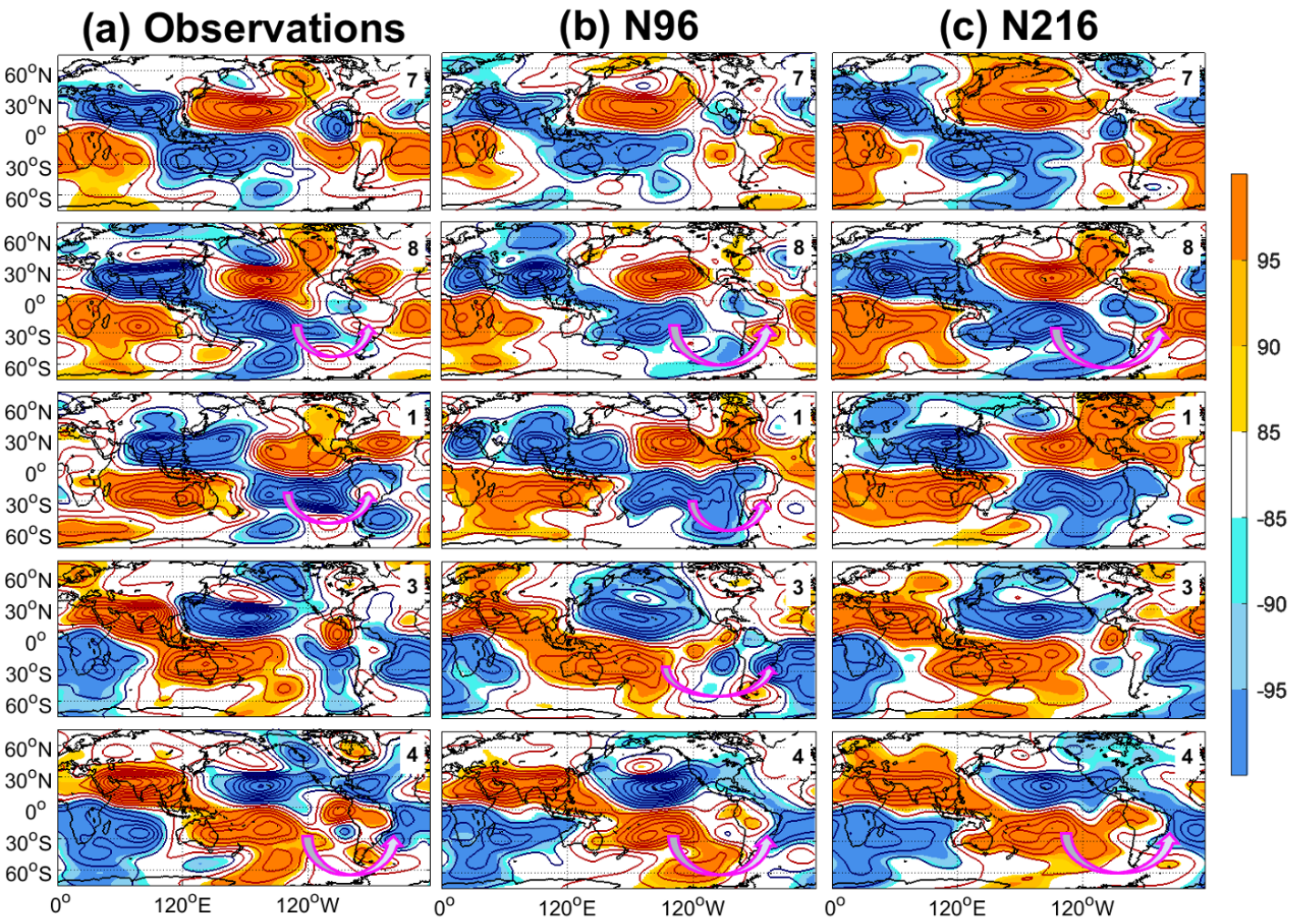
(a) Observations
(b) N96
(c) N216
60°N
30°N
0°
30°S
60°S
0°
120°E
120°W
7
8
1
3
4
95
90
85
-85
-90
-95

Figure 6.

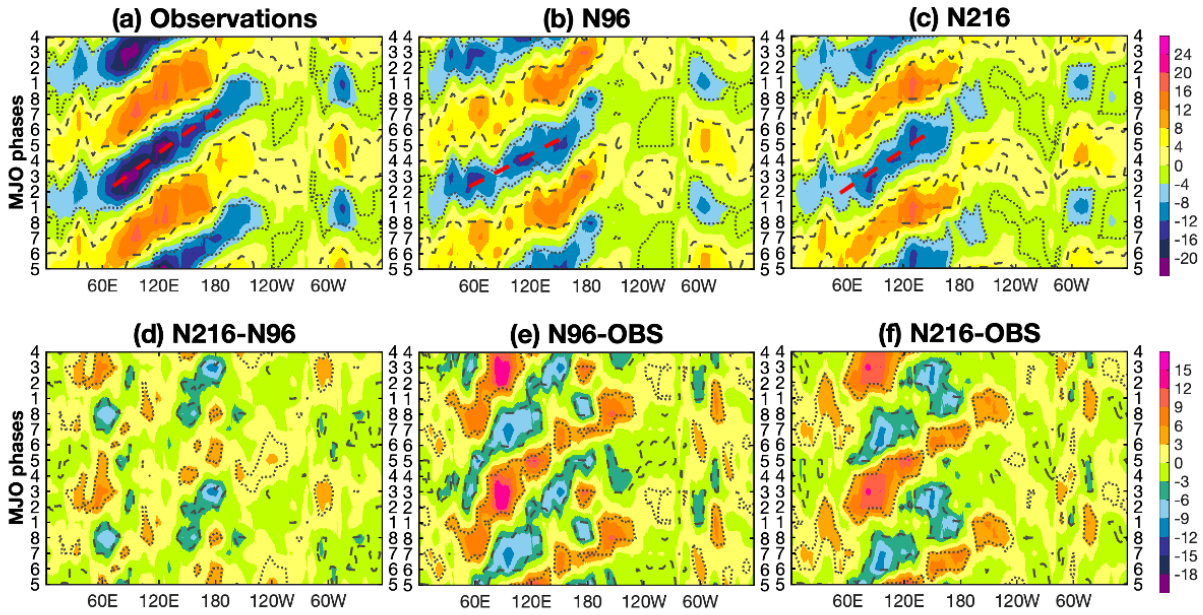
(a) Observations
(b) N96
(c) N216
(d) N216-N96
(e) N96-OBS
(f) N216-OBS
MJO phases
60E 120E 180 120W 60W
24 20 16 12 8 4 0 -4 -8 -12 -16 -20
15 12 9 6 3 0 -3 -6 -9 -12 -15 -18

Figure 7.

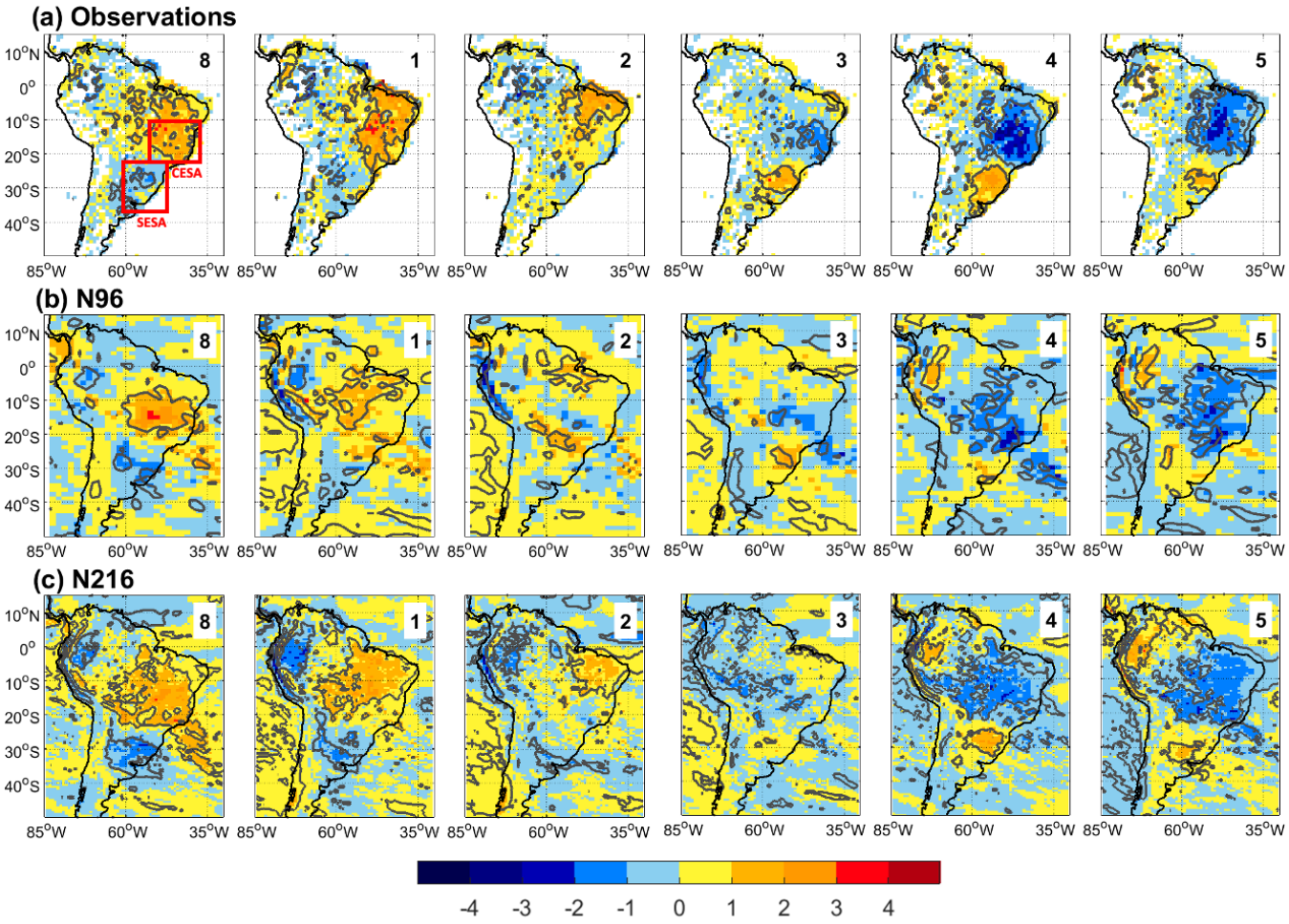
(a) Observations
(b) N96
(c) N216
8
1
2
3
4
5
CESA
SESA
10°N
0°
10°S
20°S
30°S
40°S
85°W
60°W
35°W
-4
-3
-2
-1
0
1
2
3
4

Figure 8.

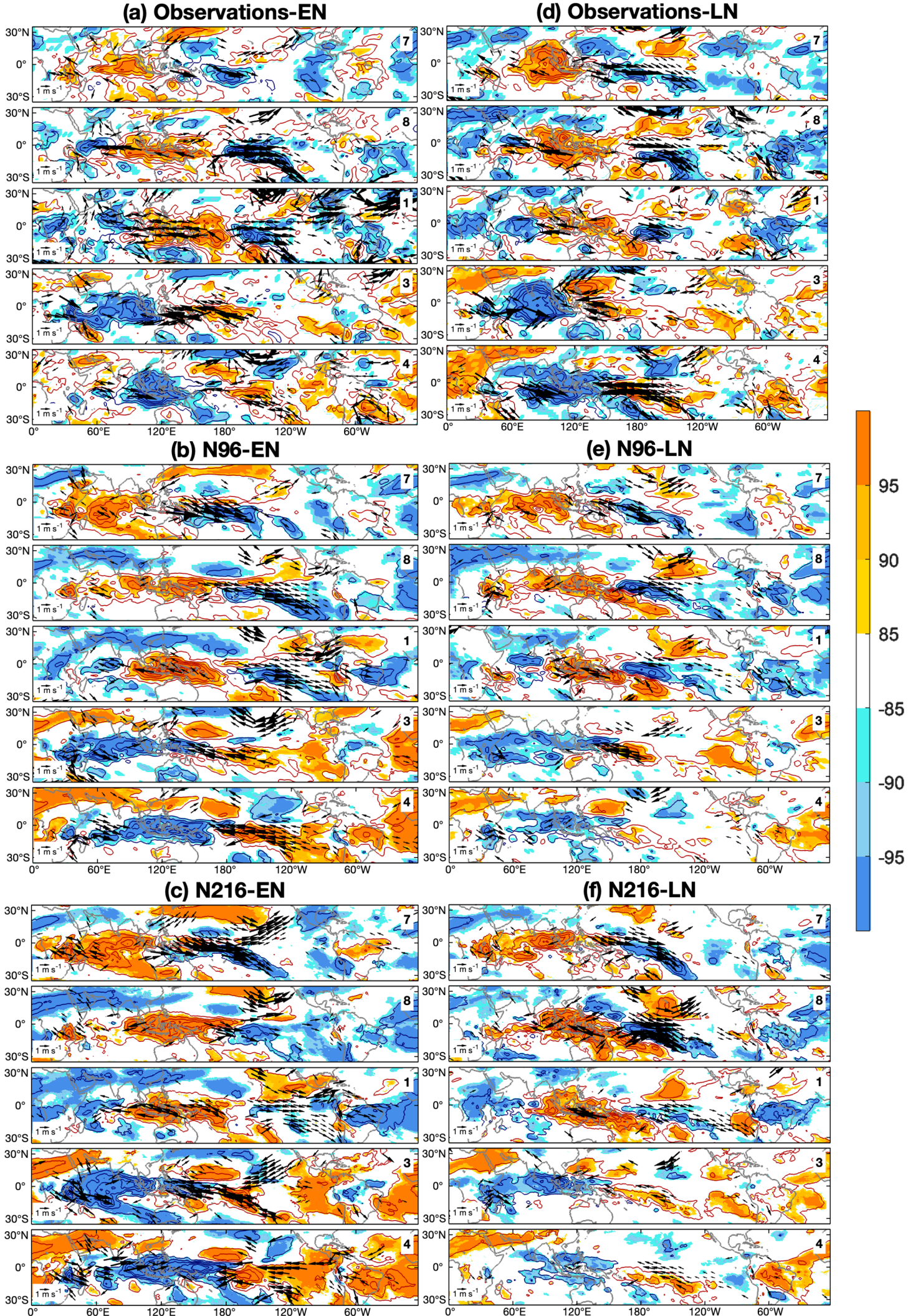
(a) Observations-EN
(d) Observations-LN
(b) N96-EN
(e) N96-LN
(c) N216-EN
(f) N216-LN
7
8
1
3
4
30°N
0°
30°S
1 m s-1
0°
60°E
120°E
180°
120°W
60°W
95
90
85
-85
-90
-95

Figure 9.

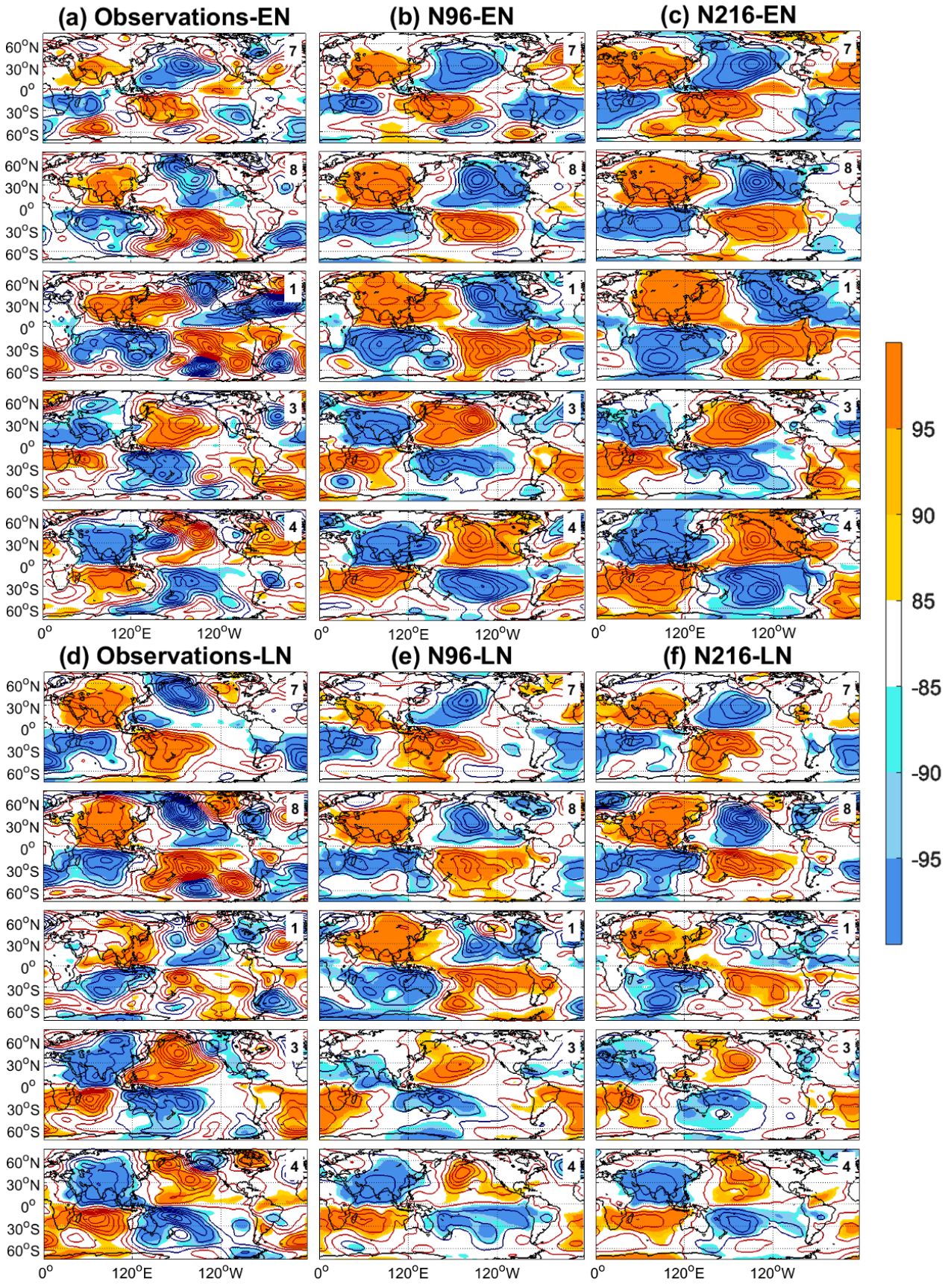
(a) Observations-EN
(b) N96-EN
(c) N216-EN
(d) Observations-LN
(e) N96-LN
(f) N216-LN
60°N
30°N
0°
30°S
60°S
0°
120°E
120°W
7
8
1
3
4
95
90
85
-85
-90
-95

Figure 10.

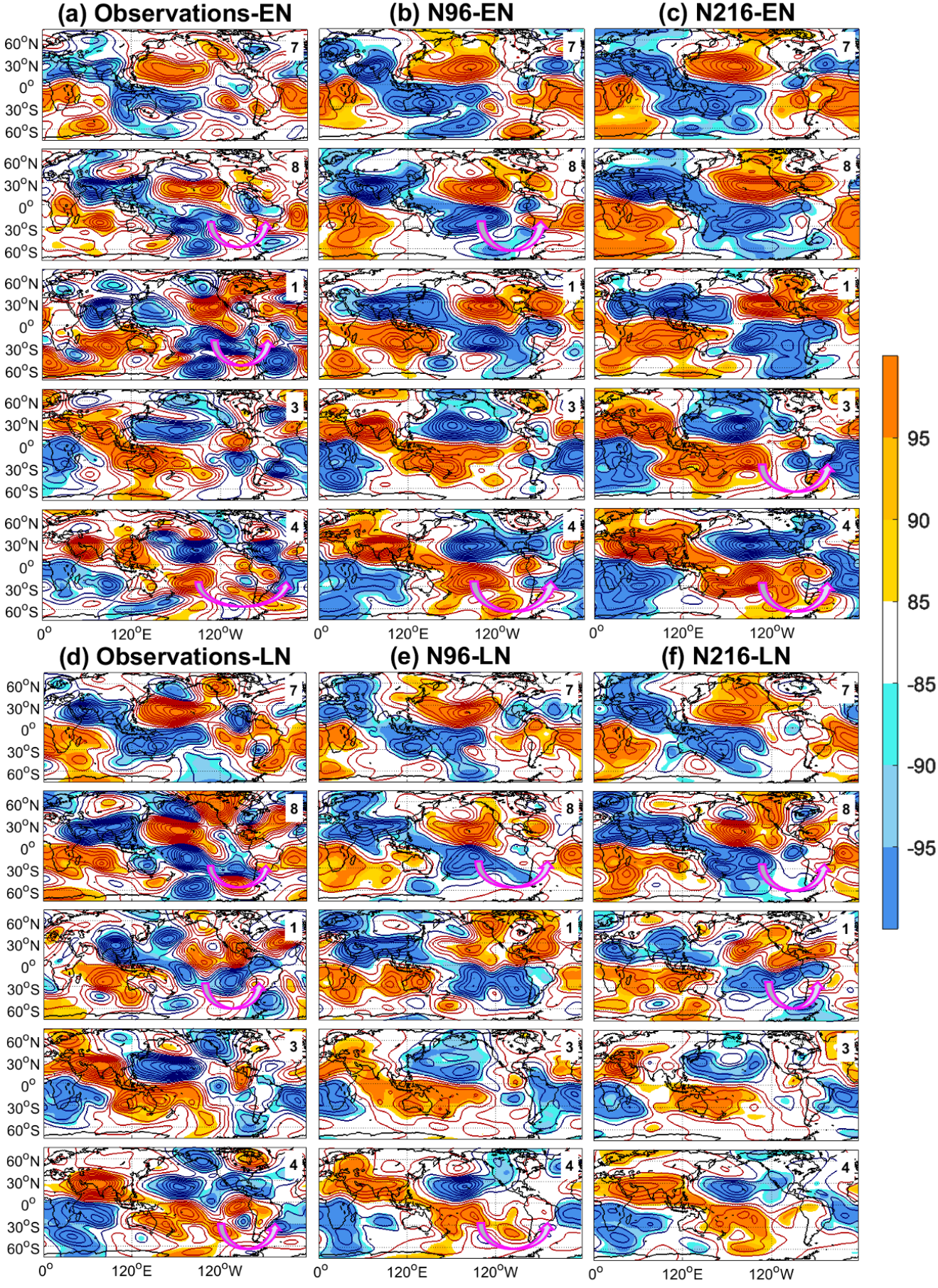
(a) Observations-EN
(b) N96-EN
(c) N216-EN
(d) Observations-LN
(e) N96-LN
(f) N216-LN
60°N
30°N
0°
30°S
60°S
0°
120°E
120°W
7
8
1
3
4
95
90
85
-85
-90
-95

Figure 11.

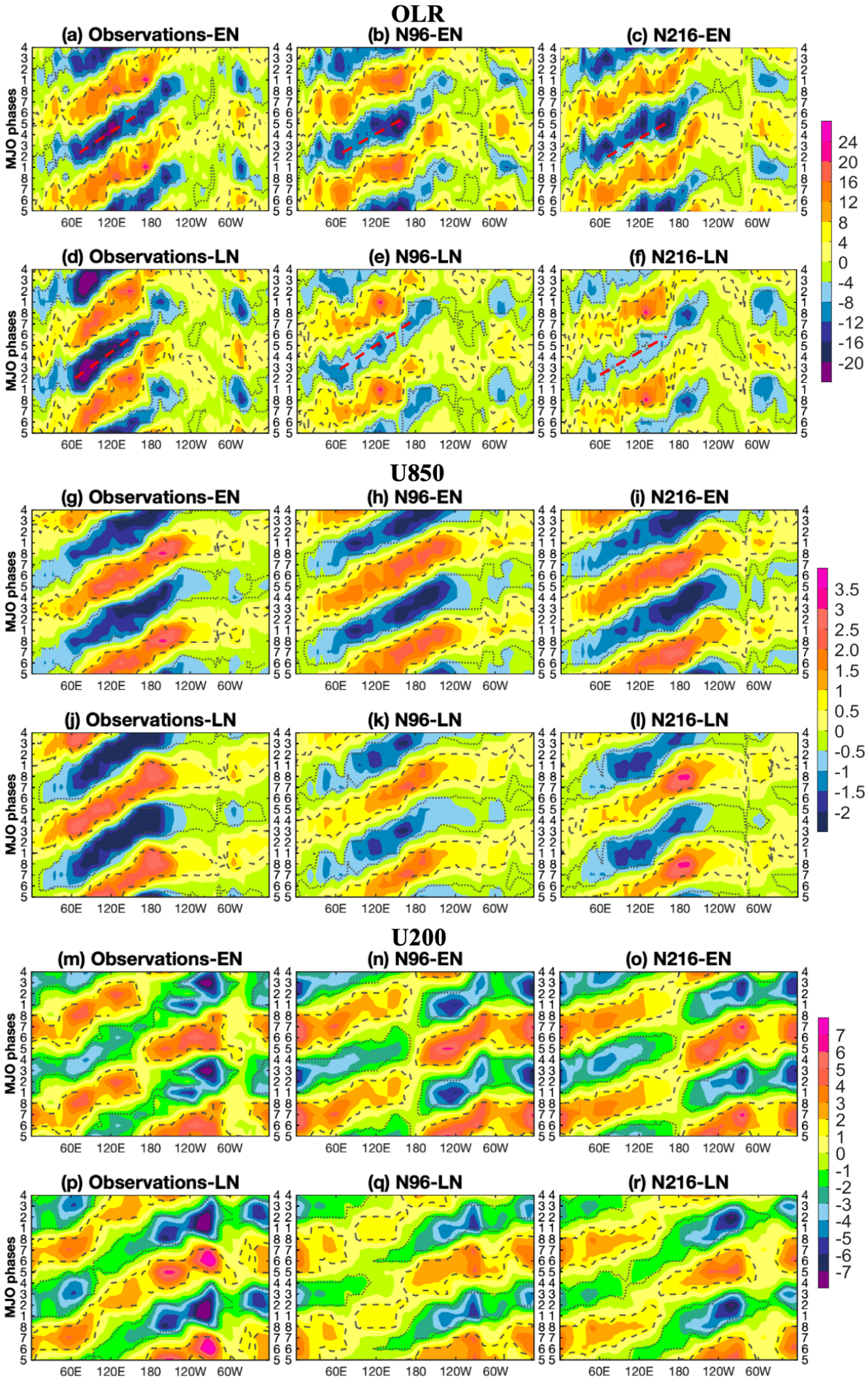
OLR
(a) Observations-EN
(b) N96-EN
(c) N216-EN
(d) Observations-LN
(e) N96-LN
(f) N216-LN
MJO phases
60E 120E 180 120W 60W
24 20 16 12 8 4 0 -4 -8 -12 -16 -20
U850
(g) Observations-EN
(h) N96-EN
(i) N216-EN
(j) Observations-LN
(k) N96-LN
(l) N216-LN
3.5 3 2.5 2.0 1.5 1 0.5 0 -0.5 -1 -1.5 -2
U200
(m) Observations-EN
(n) N96-EN
(o) N216-EN
(p) Observations-LN
(q) N96-LN
(r) N216-LN
7 6 5 4 3 2 1 0 -1 -2 -3 -4 -5 -6 -7

Figure 12.

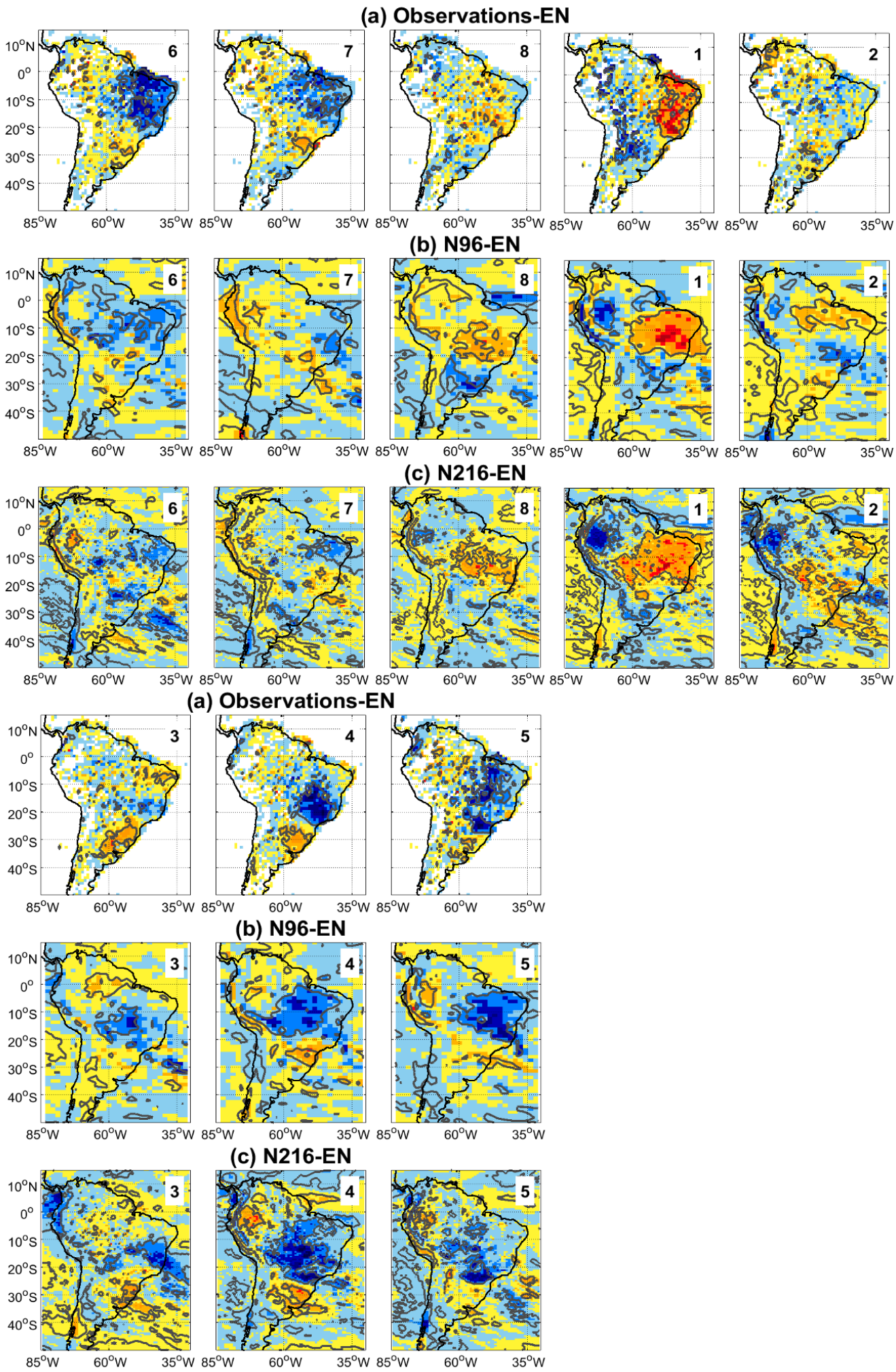
(a) Observations-EN
(b) N96-EN
(c) N216-EN
(a) Observations-EN
(b) N96-EN
(c) N216-EN
6
7
8
1
2
3
4
5
10°N
0°
10°S
20°S
30°S
40°S
85°W
60°W
35°W
-4
-3
-2
-1
0
1
2
3
4

Figure 13.

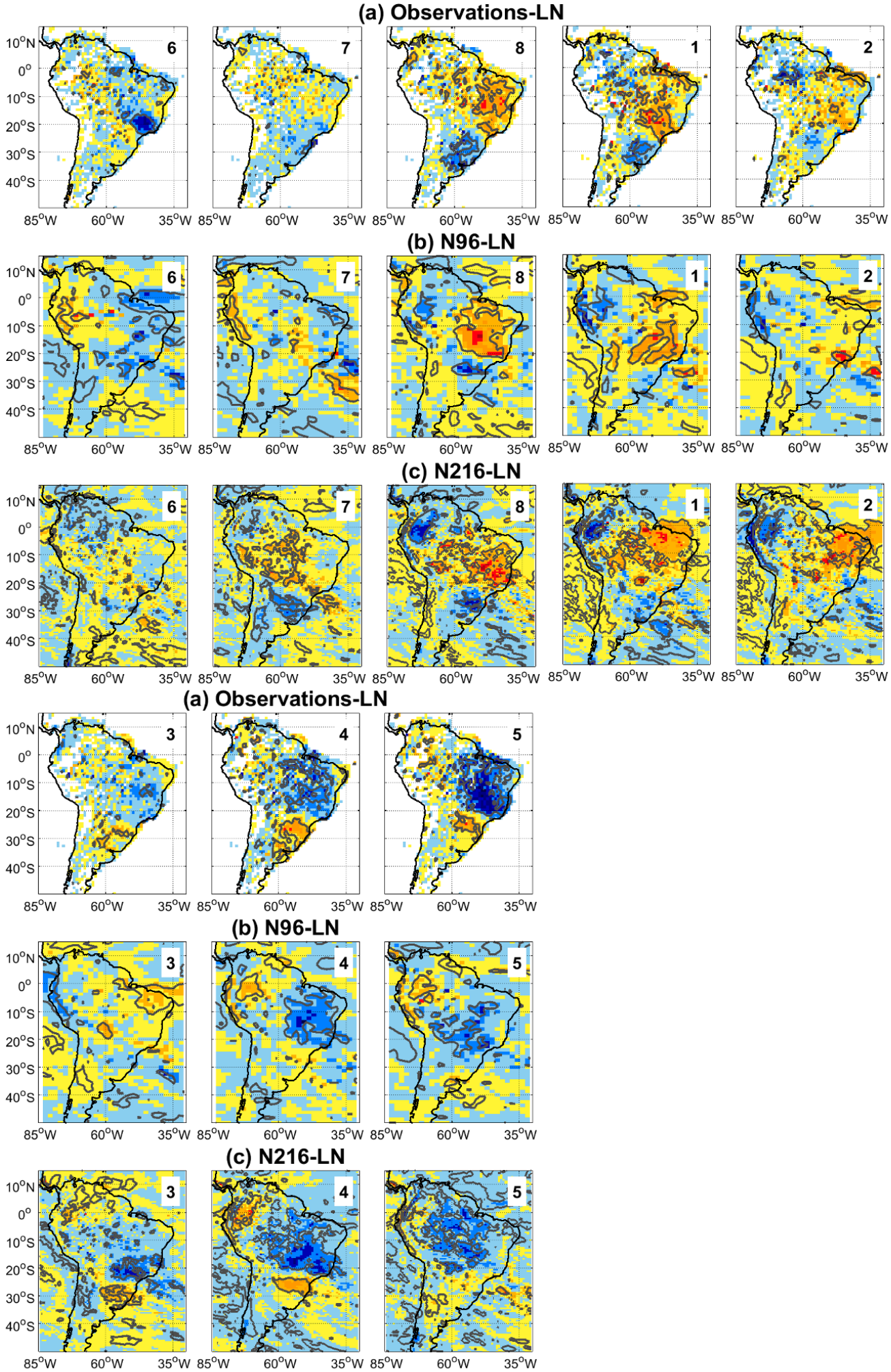
(a) Observations-LN
6
7
8
1
2
(b) N96-LN
6
7
8
1
2
(c) N216-LN
6
7
8
1
2
(a) Observations-LN
3
4
5
(b) N96-LN
3
4
5
(c) N216-LN
3
4
5
10°N
0°
10°S
20°S
30°S
40°S
85°W
60°W
35°W
-4
-3
-2
-1
0
1
2
3
4